


Modeling the diffusive dynamics of critical fluctuations near the QCD critical point

Marlene Nahrgang^{*} and Marcus Bluhm[†]

SUBATECH UMR 6457 (IMT Atlantique, Université de Nantes, IN2P3/CNRS), 4 rue Alfred Kastler, 44307 Nantes, France

 (Received 19 August 2020; accepted 6 October 2020; published 17 November 2020)

The experimental search for the QCD critical point by means of relativistic heavy-ion collisions necessitates the development of dynamical models of fluctuations. In this work, we study the fluctuations of the net-baryon density near the critical point. Due to net-baryon number conservation, the correct dynamics is given by the fluid dynamical diffusion equation, which we extend by a white noise stochastic term to include intrinsic fluctuations. We quantify finite resolution and finite-size effects by comparing our numerical results to analytic expectations for the structure factor and the equal-time correlation function. In small systems, the net-baryon number conservation turns out to be quantitatively and qualitatively important, as it introduces anticorrelations at larger distances. Including nonlinear coupling terms in the form of a Ginzburg-Landau free energy functional, we observe non-Gaussian fluctuations quantified by the excess kurtosis. We study the dynamical properties of the system close to equilibrium, for a sudden quench in temperature and a Hubble-like temperature evolution. In the real-time dynamical systems, we find the important dynamical effects of critical slowing down, weakening of the extremal value and retardation of the fluctuation signal. In this work, we establish a set of general tests, which should be met by any model propagating fluctuations, including upcoming 3 + 1 dimensional fluctuating fluid dynamics.

DOI: [10.1103/PhysRevD.102.094017](https://doi.org/10.1103/PhysRevD.102.094017)

I. INTRODUCTION

Conventional fluid dynamics propagates averages of conserved thermodynamic quantities, like the energy density or charge densities, requiring approximate local thermal equilibrium [1]. Small deviations from equilibrium are described by dissipative corrections, which are quantified by the shear and bulk viscosities and the charge conductivities or diffusion coefficients. In linear response theory, these transport coefficients are related to correlators of the fluctuations of thermodynamic quantities in the fluid dynamical limit [2,3]. By the fluctuation-dissipation theorem, it is consistent to not only include the dissipative corrections into the nonlinear fluid dynamical equations of motion but also the propagation of the corresponding intrinsic fluid dynamical fluctuations. These intrinsic fluctuations lead, e.g., to nonanalytic contributions to the time dependence of correlations [2,4–8]. But most importantly, they become especially interesting when we study the fluid dynamical behavior of a system close to a second-order phase transition [9–11].

Developing models and simulations for the real-time dynamics of fluctuations at a phase transition has become increasingly important in the field of relativistic heavy-ion

collisions. These are performed experimentally at the Large Hadron Collider (LHC) at CERN, the Relativistic Heavy-Ion Collider (RHIC) at BNL, the Super Proton Synchrotron at CERN, or the Heavy Ion Synchrotron SIS18 at GSI. In the heavy-ion collisions, strongly interacting matter at extreme temperatures T and densities is created [12–14]. The successful description of collective effects by conventional fluid dynamical simulations [15–21] and the modification of high-energetic probes measured in heavy-ion collisions compared to proton-proton collisions [22] are convincing indications for the formation of a new state of matter, the quark-gluon plasma (QGP). At the highest beam energies $\sqrt{s_{NN}}$ at the LHC, the QGP is almost baryon free, i.e., the baryochemical potential $\mu_B \simeq 0$, and the transition to hadronic matter is a crossover as demonstrated by lattice QCD calculations [23]. As the beam energy is lowered, the phase diagram of QCD can be probed at finite net-baryon density [24–28]. An especially interesting region in the phase diagram is associated with the conjectured critical point beyond which the transition to hadronic matter turns into a first-order phase transition [29–33]. Near the critical point fluctuations in conserved charges are expected to grow large and to imprint on the experimentally observed particle multiplicities in form of large event-by-event fluctuations [34–38]. Indeed, first measurements during the beam energy scan phase I at RHIC and by the HADES experiment at GSI have shown interesting features in the

^{*}marlene.nahrgang@subatech.in2p3.fr

[†]marcus.bluhm@subatech.in2p3.fr

kurtosis, a fluctuation measure associated with the fourth-order cumulant, of the net-proton distribution [39–41]. In thermodynamic, i.e., static and infinite, systems, these higher-order cumulants are known to be in particular sensitive to the growth of the correlation length of the associated critical fluctuations [42–44].

Up to this day, it is unknown quantitatively how critical fluctuations develop in real-time dynamics. Qualitatively, dynamical fluctuations of the chiral condensate or the net-baryon density, as two possible order parameters, have been studied in various works [45–68]. The lack of a more quantitative description is mainly due to the challenges that have to be met when including fluctuations in to the standard models of heavy-ion collisions; see [69] for a recent review. For the fluid dynamical description, it is rather straightforward to include criticality on the level of the equation of state [70–72], but the formulation of algorithms to treat intrinsic fluctuations in this framework remains a challenge [73–82]. For the microscopic transport models, where fluctuations are inherently present, the inclusion of a critical point remains complicated.

In this work, we study the dynamics of fluctuations in a simpler fluid dynamical model, the diffusion equation in one spatial dimension. Our main intent is to report the development of an algorithm, which treats fluctuations for the crucial long-wavelength modes reliably, and to present corresponding benchmark tests that should be met by all future approaches that deal with fluid dynamical fluctuations. We focus on the net-baryon density, which in the long-time limit becomes the critical mode associated with the critical point in QCD. We include the critical physics in the vicinity of the QCD critical point by a Ginzburg-Landau free energy functional, motivated by the three-dimensional Ising universality class. We then test the presented algorithm for the linear Gaussian limits in equilibrium. Here, in particular, the static structure factor and the equal-time correlation function are useful quantities for probing the dynamics of the fluctuations. We then evaluate the dynamical properties of the system by looking at the dynamic structure factor in equilibrium first. Here, we recover the expected dynamical universality class of model B [9]. Next, we investigate the scenario of a sudden temperature quench and finally a Hubble-like evolution of the temperature. We observe effects of critical slowing down, a weakening and a retardation of the maximal signal.

II. DIFFUSIVE DYNAMICS NEAR THE QCD CRITICAL POINT

The equations of relativistic fluid dynamics describe the conservation of energy and momentum and of net-charges via

$$\partial_\mu T^{\mu\nu} = 0, \quad (1)$$

$$\partial_\mu N_i^\mu = 0. \quad (2)$$

For our purpose, we focus on the nonrelativistic evolution of the net-baryon number current $N_B^\mu = n_B u^\mu + j_B^\mu$, where the Navier-Stokes expression for the viscous current is given by

$$j_B^\mu = -\Gamma T \Delta^{\mu\nu} \partial_\nu \left(\frac{\mu_B}{T} \right), \quad (3)$$

with $\Delta^{\mu\nu} = u^\mu u^\nu - g^{\mu\nu}$, fluid velocity u^μ , and mobility coefficient Γ . We consider a system that is decoupled from the fluid velocity field which we assume to be space-time independent. In this case, we recover the diffusion equation

$$\partial_t n_B = \Gamma T \nabla^2 \left(\frac{\mu_B}{T} \right) \quad (4)$$

for the net-baryon density n_B . The diffusive dynamics happens such as to minimize the free energy in the system. With the thermodynamic relation $\mu_B = \delta\mathcal{F}/\delta n_B$, one obtains the diffusion equation generated by the variation of the free energy functional \mathcal{F} for a system of spatially homogeneous temperature

$$\partial_t n_B = \Gamma \nabla^2 \left(\frac{\delta\mathcal{F}[n_B]}{\delta n_B} \right). \quad (5)$$

Since we are interested in the dynamics of intrinsic fluctuations near the critical point, we include a stochastic term to arrive at the stochastic diffusion equation

$$\partial_t n_B = \Gamma \nabla^2 \left(\frac{\delta\mathcal{F}[n_B]}{\delta n_B} \right) + \vec{\nabla} \cdot \vec{J}, \quad (6)$$

where \vec{J} is a stochastic current given by

$$\vec{J} = \sqrt{2T\Gamma} \vec{\zeta}, \quad (7)$$

and $\vec{\zeta}$ is a Gaussian spatiotemporal white noise field with zero mean and unit variance. Fulfilling the fluctuation-dissipation theorem, the covariance of the stochastic term guarantees that the long-time equilibrium distribution is given by

$$P_{\text{eq}}[n_B] = \frac{1}{\mathcal{Z}} \exp\left(\frac{-\mathcal{F}[n_B]}{T} \right), \quad (8)$$

normalized by the partition function \mathcal{Z} .

We choose the free energy functional near the QCD critical point to be of the following polynomial form in $\Delta n_B = n_B - n_c$ with critical density n_c :

$$\mathcal{F}[n_B] = T \int d^3x \left(\frac{m^2}{2n_c^2} (\Delta n_B)^2 + \frac{K}{2n_c^2} (\nabla n_B)^2 + \frac{\lambda_3}{3n_c^3} (\Delta n_B)^3 + \frac{\lambda_4}{4n_c^4} (\Delta n_B)^4 + \frac{\lambda_6}{6n_c^6} (\Delta n_B)^6 \right). \quad (9)$$

We note that the chosen Ginzburg-Landau form for the critical part of the free energy \mathcal{F} may be augmented by regular contributions. The coupling coefficients can be calculated through the mapping of the three-dimensional Ising spin model onto a universal effective potential [83,84]. This determines the dependence of these couplings on the thermodynamic correlation length ξ within the given universality class as

$$m^2 = \frac{1}{\xi_0 \xi^2}, \quad (10)$$

$$K = \tilde{K}/\xi_0, \quad (11)$$

$$\lambda_3 = n_c \tilde{\lambda}_3 (\xi/\xi_0)^{-3/2}, \quad (12)$$

$$\lambda_4 = n_c \tilde{\lambda}_4 (\xi/\xi_0)^{-1}, \quad (13)$$

$$\lambda_6 = n_c \tilde{\lambda}_6. \quad (14)$$

In principle, the dimensionless couplings $\tilde{\lambda}_3$, $\tilde{\lambda}_4$, and $\tilde{\lambda}_6$ have universal values as well, but the uncertainty in translating the spin variables to the QCD phase diagram leads to rather unknown values for these couplings. We will use $\tilde{\lambda}_3 = 1$, $\tilde{\lambda}_4 = 10$, and $\tilde{\lambda}_6 = 3$ in this work. This implies that the temperature dependence of the couplings is determined entirely by the behavior of ξ established through a matching to the susceptibility of the Ising model scaling equation of state [85]. In the work [83,84], it turned out to be important to include the λ_6 coupling in order to describe the probability distribution of the fluctuations in the spin model. We therefore include this term in our study as well, although in a perturbative expansion in ξ^3/V with volume V this term is suppressed in the scaling regime [42,86].

As can be seen in Fig. 1, the thermodynamic correlation length peaks around T_c which we choose as $T_c = 0.15$ GeV, while the couplings λ_3 and λ_4 have a minimum at T_c . There is a region around T_c where the nonlinear couplings λ_4 and λ_6 are larger than the Gaussian mass parameter m . We expect nonlinear effects to be largest here. The critical net-baryon density n_c depends on the location of the critical point and the equation of state. The net-baryon density at chemical freeze-out as a function of $\sqrt{s_{\text{NN}}}$ was obtained from statistical model fits using the hadron resonance gas model in [87]. Here, maximal values of $n_B = 0.12/\text{fm}^3$ are reached at $\sqrt{s_{\text{NN}}} \sim 4$ GeV. During the evolution, the system can reach much higher local values of $n_B = 5\rho_0$ with $\rho_0 = 0.16/\text{fm}^3$ [88]. In this work, we choose a value of $n_c = 1/(3\text{fm}^3)$.

The above described setup is in general designed for studying the diffusion dynamics of critical fluctuations in three spatial dimensions. The numerical framework presented here focusses on the dynamics restricted to one spatial direction. For this purpose, we scale out the

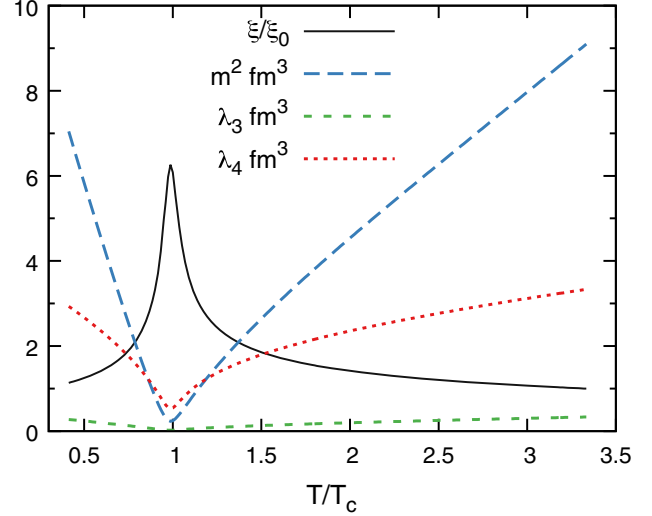


FIG. 1. Scaled temperature dependence of the parameters in the Ginzburg-Landau free energy functional \mathcal{F} in Eq. (9). We choose $T_c = 0.15$ GeV and $\xi = \xi_0 = 0.479$ fm at $T = T_0 = 0.5$ GeV. Furthermore, the coupling $\lambda_6 = 1/\text{fm}^3$ (not shown) is set constant as a function of T . The temperature dependence of ξ/ξ_0 , which serves as input for the parameters in this work, follows from a matching to the susceptibility of the Ising model scaling equation of state for constant μ_B on the crossover side of the QCD phase diagram; see [89,90] for some details.

transverse area A and consider the dynamics only in the longitudinal direction which resembles the situation met in a highly anisotropic heavy-ion collision. With this, the stochastic diffusion equation (6) becomes

$$\begin{aligned} \partial_t n_B(x, t) &= \frac{D}{n_c} (m^2 \nabla_x^2 n_B - K \nabla_x^4 n_B) \\ &+ D \nabla_x^2 \left(\frac{\lambda_3}{n_c^2} (\Delta n_B)^2 + \frac{\lambda_4}{n_c^3} (\Delta n_B)^3 + \frac{\lambda_6}{n_c^5} (\Delta n_B)^5 \right) \\ &+ \sqrt{2Dn_c/A} \nabla_x \zeta_x(x, t), \end{aligned} \quad (15)$$

where we have expressed the mobility coefficient $\Gamma = Dn_c/T$ via the diffusion coefficient D and the covariance reads $\langle \zeta_x(x, t), \zeta_x(x', t') \rangle = \delta(x - x') \delta(t - t')$.

III. EQUILIBRIUM FLUCTUATIONS

In this section, we investigate the long-time limit for the stochastic diffusion of the net-baryon density at various fixed thermal conditions. For this purpose, we consider a system in a quasi one-dimensional box of length L with periodic boundary conditions. Initially, the net-baryon density is constant and set to $n_B(x) = n_c$. Both, the discretization with $\Delta x = L/N_x$ (N_x is the number of sites) and the finite size of the box will introduce effects which make the results differ from the continuum limit ($\Delta x \rightarrow 0$) and the thermodynamic limit ($L \rightarrow \infty$). While the limited

resolution is a technical issue, the finite size reflects the situation of the fireball created in a heavy-ion collision. After initialization, we let the system equilibrate during a long time, which is proportional to L^2/D , before evaluating the physical observables such as the variance and kurtosis or the equal-time correlation function and structure factor of the system. These are related to the equilibrium distribution which is an invariant measure and independent of D . The latter is exemplarily set to $D = 1$ fm.

We note that the determination of equilibrium results, i.e., the long-time behavior, numerically requires a significant amount of statistics. For dissipation in form of diffusion, any memory on initial conditions is eventually lost and the fluctuation-dissipation balance guarantees ergodicity of the system. This implies that ensemble averages can be either obtained by averaging over multiple samples or equally by averaging over time after performing a sufficient amount of equilibration steps proportional to $L^2/(D\Delta t)$. In this work, the high-statistics equilibrium results have been obtained by combining both methods.

We solve the stochastic diffusion equation (15) numerically within a semi-implicit scheme, where the nonlinear terms in Δn_B are treated explicitly. Charge conservation is respected with very high precision by imposing periodic boundary conditions. More details can be found in the Appendix A.

A. Static structure factor and equal-time correlation function in Gaussian models

The stochastic diffusion equation Eq. (15) contains different physics cases. For the Gaussian models, the nonlinear couplings λ_i are equal to zero. In this case, exact analytic continuum expressions for prominent physical observables are calculable. One of these represents the dynamic structure factor $S(k, \omega)$ for wave vector \vec{k} and frequency ω . It follows directly from the space-time Fourier transform of the stochastic diffusion equation as

$$\begin{aligned} S(k, \omega) &\equiv V \langle \Delta \hat{n}_B(k, \omega) \Delta \hat{n}_B^*(k, \omega) \rangle \\ &= \frac{2Dn_c k^2}{\omega^2 + [Dk^2(m^2 + Kk^2)/n_c]^2} \end{aligned} \quad (16)$$

and entails the dynamical space-time spectrum of the fluctuating net-baryon density. We note that for the spatio-temporal white noise field the dynamic structure factor is $S_{\xi_x}(k, \omega) = L \langle \hat{\xi}_x \hat{\xi}_x^* \rangle = 1$. From $S(k, \omega)$, the spatial spectrum at equal time, i.e., the static structure factor $S(k)$, follows from integration over all ω as

$$S(k) = \frac{1}{2\pi} \int_{-\infty}^{\infty} S(k, \omega) d\omega. \quad (17)$$

The simplest version of a Gaussian model is obtained when $\tilde{K} = \tilde{\lambda}_3 = \tilde{\lambda}_4 = \tilde{\lambda}_6 = 0$ in Eq. (9). In this case, we are

left with the Gaussian mass term which gives rise to the standard diffusion equation. This model serves as a reference and was discussed in detail in [64], where the correct numerical implementation of Eq. (15) for this case was verified. From Eq. (15), the static structure factor for $\tilde{K} = 0$ follows via Eq. (17) as

$$S(k) = \frac{n_c^2}{m^2}, \quad (18)$$

which is independent of the wave vector \vec{k} . Contrary to simple Euler schemes, the semi-implicit scheme applied in our framework achieves highest accuracy for all wave numbers independent of the time step Δt . As we show in Appendix B, the corresponding structure factor in discretized space-time S_k coincides with Eq. (18) and is therefore independent of the lattice spacing Δx . In [64], we verified that this is reproduced in our framework.

The version with a term of nonzero \tilde{K} , which describes a kinetic energy in a Klein-Gordon type action or a surface tension in diffusion equations, can still be solved analytically in the continuum. In this case, which we will call Gauss + surface model, the static structure factor is given by

$$S(k) = \frac{n_c^2}{m^2} \frac{1}{1 + Kk^2/m^2}. \quad (19)$$

Due to the finite surface tension, the amplitude of the fluctuations becomes suppressed with increasing k .

The numerical results presented in this work have been obtained for $\tilde{K} = 1$ in each of the calculations. For our numerical framework, the static structure factor for the Gauss + surface model in discretized space-time reads (see Appendix B)

$$S_k = \frac{n_c^2}{m^2} \frac{1}{1 + \frac{2K}{m^2 \Delta x^2} [1 - \cos(k\Delta x)]}. \quad (20)$$

With increasing resolution, $\Delta x \rightarrow 0$, this result converges to Eq. (19). In Fig. 2, we show the numerical results for the static structure factor S_k as a function of wave number κ for fixed box length $L = 10$ fm and different resolutions at two different temperatures. As the considered box is finite in size and the resolution limited by N_x , only a finite number of modes with discrete $\kappa = kL/(2\pi)$ is realized. Our numerical implementation reproduces the analytic expectations for S_k from Eq. (20); thus, resolution effects are well understood. We note that for a resolution of $\Delta x = (10/128)$ fm the static structure factor starts to deviate visibly from the continuum result only for $\kappa \gtrsim 25$ while for the modes $\kappa \lesssim 10$, which are important for the critical physics, the continuum limit is reached. Close to T_c , the amplitude of fluctuations for modes with small κ is

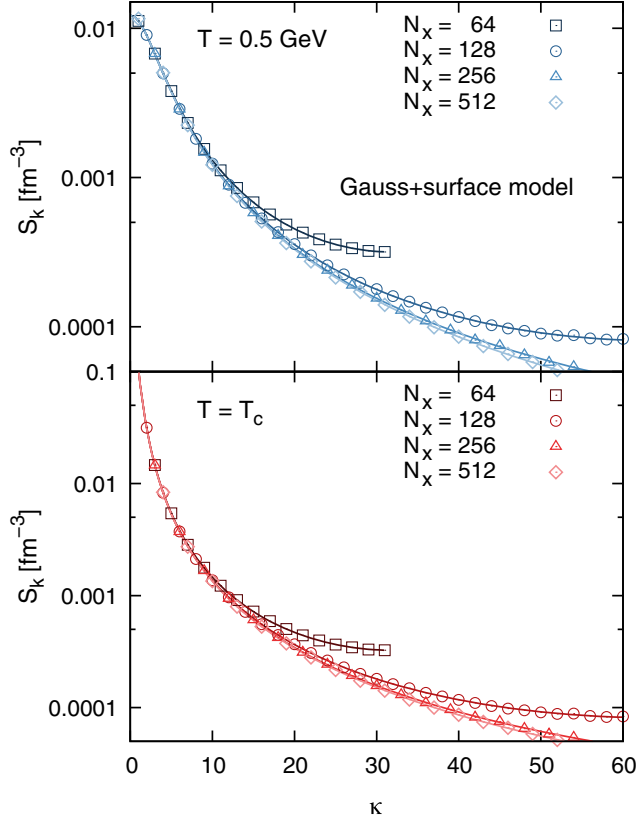


FIG. 2. The static structure factor (symbols) as a function of wave number κ in the Gauss + surface model ($\lambda_3 = \lambda_4 = \lambda_6 = 0$) for different $N_x = 64, 128, 256, 512$ and fixed $L = 10$ fm. For both temperatures, $T = 0.5$ GeV and $T = T_c$, the theoretical expectations (solid curves) for the static structure factor in discretized space-time S_k , Eq. (20) with $k = 2\pi\kappa/L$, are perfectly reproduced. Because of the Hermitian symmetry between κ and $N_x - \kappa$, S_k is symmetric about $\kappa = N_x/2$. With increasing resolution, S_k approaches the continuum result $S(k)$ in Eq. (19).

increased compared to temperatures further away while S_k is rather independent of T for larger wave numbers.

Another prominent observable is the equal-time correlation function of density fluctuations in coordinate space. In the continuum limit, it is defined as the Fourier transform of the static structure factor $S(k)$ in Eq. (17) via

$$\langle \Delta n_B(r) \Delta n_B(0) \rangle = \int \frac{d^d k}{(2\pi)^d} e^{i\vec{k}\cdot\vec{r}} S(k). \quad (21)$$

For the quasi $d = 1$ dimensional system studied in our work, the equal-time correlation function of density fluctuations in the longitudinal direction is given for the Gauss + surface model by

$$\langle \Delta n_B(r) \Delta n_B(0) \rangle = \frac{n_c^2}{2Am\sqrt{K}} \exp\left(-r \frac{m}{\sqrt{K}}\right). \quad (22)$$

For $\tilde{K} = 1$, we recover the standard relation between the Gaussian mass parameter and the correlation length given

by Klein-Gordon theory. The truly realized correlation length in the system depends, however, in general on the surface tension. The integral of Eq. (22) over distances much larger than the correlation length yields the full weight of the fluctuation, $n_c^2/(Am^2)$. This is the same as for the pure Gaussian model with vanishing \tilde{K} , where Eq. (22) reduces to $\langle \Delta n_B(r) \Delta n_B(0) \rangle = (n_c^2/(Am^2))\delta(r)$ and the expected uncorrelated Gaussian limit is recovered.

In [64], the behavior of $\langle \Delta n_B(r) \Delta n_B(0) \rangle$ for the pure Gaussian model was studied numerically. For this model, the correlation function in discretized space-time is given by $\langle (\Delta n_B)_j (\Delta n_B)_l \rangle = n_c^2/(Am^2 \Delta x) \delta_{jl}$, where j, l can go over all cells. Accordingly, fluctuations are uncorrelated over distances larger than the lattice spacing. In our simulations, exact net-baryon number conservation is realized over the entire box of finite length L . This leads to corrections which can analytically be understood by imposing the condition of charge conservation $\sum_l \langle (\Delta n_B)_j (\Delta n_B)_l \rangle = 0$ for any j ; see Appendix C. Correspondingly, the expectation for the equal-time correlation function changes to

$$\langle (\Delta n_B)_j (\Delta n_B)_l \rangle = \frac{n_c^2}{Am^2} \left(\frac{\delta_{jl}}{\Delta x} - \frac{1}{L} \right), \quad (23)$$

which amounts to a constant negative shift that vanishes with increasing L for fixed resolution. This behavior was found to be perfectly reproduced in the numerics; see [64].

For the Gauss + surface model, similar considerations can be made. Numerical results for the equal-time correlation function $\langle (\Delta n_B)_j (\Delta n_B)_l \rangle$ as a function of scaled distance $r/\Delta x = |j - l|$ are shown in Fig. 3 for fixed resolution Δx and various L at two different temperatures. We find that the equal-time correlation function is shifted to negative values at large distances r demonstrating significant anticorrelations. With increasing box size L at fixed resolution, the negative shift becomes less pronounced. This behavior is a consequence of exact net-baryon number conservation; see Appendix C. Taking the latter into account, cf. Eq. (C4), the corresponding analytic expectations agree well with our numerical results; thus, finite-size effects in connection with exact charge conservation are well under control.

For temperatures close to T_c , $\langle (\Delta n_B)_j (\Delta n_B)_l \rangle$ becomes broader and correlations form over larger distances as one expects from the continuum expression in Eq. (22). Nonetheless, this depends strongly on the size of the box and finite-size effects in connection with charge conservation clearly affect the development of the correlations. We note that for the larger systems the equilibration times become very long and increasing computer resources are needed to produce equilibrated systems and build up the expected long-range correlations. In fact, the tiny deviation between theoretical expectations and numerical results at large r seen in Fig. 3 at $T = T_c$ for $L = 40$ fm is the result

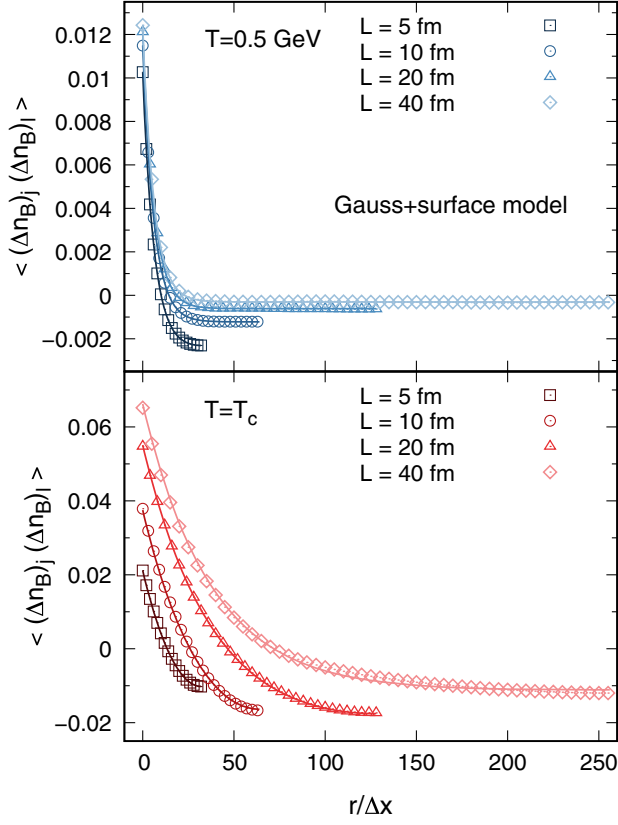


FIG. 3. The equal-time correlation function of density fluctuations (symbols) in the Gauss + surface model ($\lambda_3 = \lambda_4 = \lambda_6 = 0$) for different $L/\text{fm} = 5, 10, 20, 40$, fixed $\Delta x = (20/256)$ fm, i.e., different N_x , and a representative $A = 1$ fm². For both temperatures, $T = 0.5$ GeV and $T = T_c$, the numerical results are found to perfectly agree with the theoretical expectations (solid curves) when including the finite-size corrections for exact net-baryon number conservation, cf. Appendix C. The correlation function is symmetric in $r = |j - l|\Delta x$ about $r = L/2$.

of an insufficient equilibration before evaluating the equal-time correlation function.

B. Static structure factor and equal-time correlation function in the Ginzburg-Landau model

Let us now study the impact of the nonlinear coupling terms in what we call the Ginzburg-Landau model on the static structure factor and the equal-time correlation function. This is shown in Fig. 4 in comparison with the Gauss + surface model results for a system of $L = 20$ fm with $N_x = 256$ at $T = T_c$. One observes that the influence of the nonzero λ_i is the significant reduction of S_k at small wave numbers κ while it is less important for larger κ . This reduction of the amplitude of fluctuations at long wavelengths is also reflected in the development of spatial correlations. With nonzero λ_i , the equal-time correlation function is less broad and long-range correlations are suppressed. In addition, correlations at small distances are less pronounced which consequently reduces the

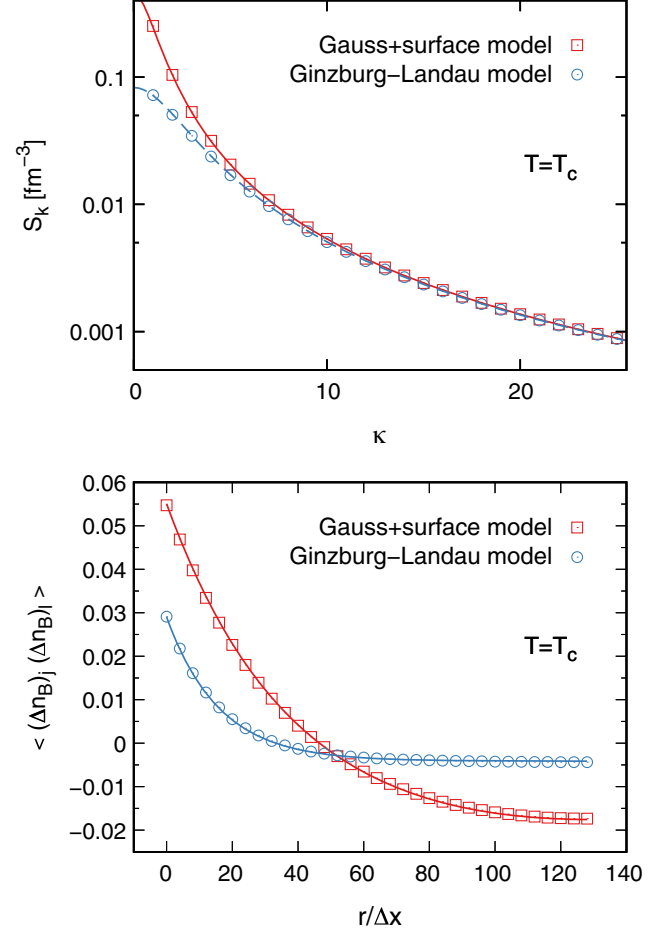


FIG. 4. Comparison of the static structure factor (upper panel) and the equal-time correlation function of density fluctuations (lower panel) between Ginzburg-Landau model (circles) and Gauss + surface model (squares) for a system of $L = 20$ fm, $N_x = 256$ and $A = 1$ fm² at $T = T_c$. The theoretical expectations in the Gauss + surface model (solid red curves), see Sec. III A, agree with the numerics. The numerical results of the Ginzburg-Landau model can formally be described by the same analytic expressions when replacing m by an effective mass m_{eff} that is fitted to describe S_k (dashed blue curves).

quantitative impact of exact charge conservation in the finite-size system. These effects are found to be less important for T further away from T_c .

The numerical results of the Gauss + surface model can successfully be described by our analytic expectations in discretized space-time; see Sec. III A. For the Ginzburg-Landau model, instead, no exact analytic expressions can be derived to compare the numerics with. We note, however, that the numerical results of the Ginzburg-Landau model on the level of two-point correlations can formally be described by the analytic expressions of the Gauss + surface model but with a modified Gaussian mass parameter while K is kept fixed. This effective mass, m_{eff} , is larger than m of the Gauss + surface model for any T . Near T_c the relative increase of m_{eff} with respect to m is stronger. For the systems

studied in this work, we find no additional Δx -dependence in m_{eff} within the statistical uncertainty.

C. Temperature and system-size dependence of the correlation length

The continuum expectation of the equal-time correlation function in the Gauss + surface model for an infinite system is given in Eq. (22). The numerical results in discretized space resemble this form of an exponential decay. This is also the case when taking nonzero λ_i into account. As we have seen in Figs. 3 and 4, net-baryon number conservation in the finite-size system results in a negative offset signaling anticorrelations. Still, an exponential form of the correlation function remains. Therefore, we may fit the numerical results of the Gauss + surface and Ginzburg-Landau models with an ansatz that contains the exponential behavior and the offset (see Appendix D for details) in order to determine the correlation length $\tilde{\xi}$. The latter depends besides T in particular on the system size L and can be different from the thermodynamic correlation length ξ .

In Fig. 5, we show the system-size dependence of the fitted $\tilde{\xi}$ in the Gauss + surface and Ginzburg-Landau models for two different T at fixed resolution $\Delta x = (20/256)$ fm. The residual Δx -dependence can be estimated to be on the percent level for all T and L . For the parameters studied in this work, cf. Fig. 1, the maximally reached thermodynamic correlation length in an infinite system, ξ , is about 3 fm near T_c and minimally we have $\xi = \xi_0$ at $T = 0.5$ GeV. These values are indicated by the gray dotted lines in Fig. 5. For $T = 0.5$ GeV (open squares and circles), a system size of $L = 5$ fm is already sufficient for $\tilde{\xi}$ to reach approximately the value of ξ . This remains unchanged with increasing L . However, for all other T with a larger ξ , charge conservation turns out to be important, particularly in the smaller systems. In fact, it can lead to a sizable reduction of $\tilde{\xi}$ compared to ξ for $L = 5$ fm. This effect is pronounced strongest at T_c (solid squares and circles). For $T = T_c$, the fitted correlation length increases strongly toward ξ with increasing L for the Gauss + surface model. For $L = 40$ fm, one finds $\tilde{\xi}$ to be approximately ξ . In contrast, in the Ginzburg-Landau model, $\tilde{\xi}$ remains always small compared to ξ and shows within the statistics a negligible system-size dependence for $L \geq 10$ fm. This reduction is entirely a consequence of the nonlinear interactions.

In Fig. 6, we compare for $L = 20$ fm the fitted correlation length as a function of temperature with ξ . One observes that $\tilde{\xi}$ is approximately ξ in the Gauss + surface model for all T except very close to T_c , where finite-size and charge-conservation effects are strongest, cf. Fig. 5. From this observation, we conclude that in order to draw physical conclusions a reasonable compromise between finite-resolution and finite-size effects on the one hand and limited computational resources on the other hand is to

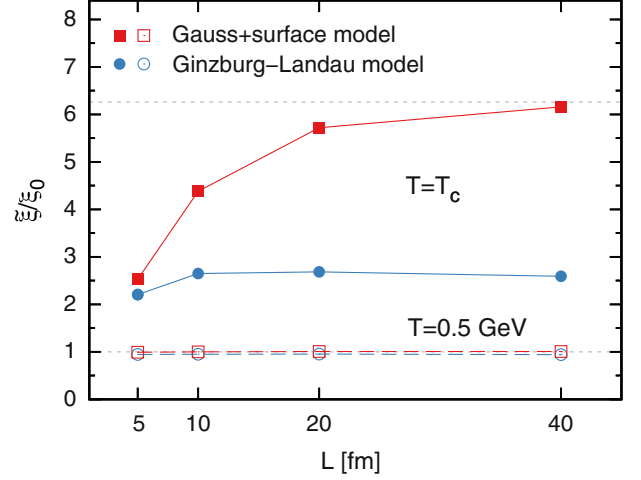


FIG. 5. L -dependence of the correlation length $\tilde{\xi}$ in units of ξ_0 in the Gauss + surface (squares) and Ginzburg-Landau (circles) models at fixed resolution $\Delta x = (20/256)$ fm for two different temperatures, $T = 0.5$ GeV (open symbols) and $T = T_c$ (solid symbols). The horizontal, gray dotted lines show for comparison the corresponding scaled thermodynamic correlation length ξ/ξ_0 for an infinite system, cf. the input parameters in Fig. 1.

study systems of $L = 20$ fm and $N_x = 256$ in this work. The presence of the nonlinear interactions in the Ginzburg-Landau model impacts the development of long-range correlations significantly. For all T , we find a $\tilde{\xi}$ which is smaller in the Ginzburg-Landau model than in the Gauss + surface model. While far away from T_c the effect is tiny, the reduction is visible in the vicinity of T_c . This behavior is in line with the temperature dependence of the parameters, see Fig. 1, and with the observation that for describing the structure factor and the correlation function in the

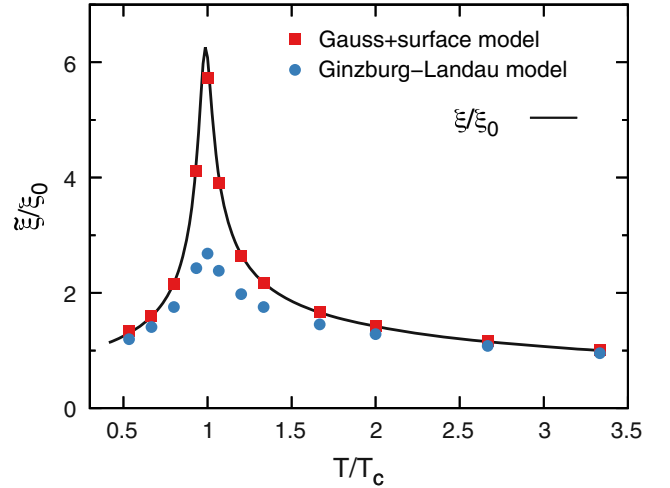


FIG. 6. Comparison of the scaled temperature dependence of the correlation length $\tilde{\xi}$ in units of ξ_0 in the Gauss + surface (squares) and Ginzburg-Landau (circles) models with the scaled thermodynamic correlation length ξ/ξ_0 for an infinite system (solid line) for simulations with $L = 20$ fm and $\Delta x = L/256$.

Ginzburg-Landau model by the analytic expressions of the Gauss + surface model one needs $m_{\text{eff}} > m$. In fact, we find that m_{eff}/m behaves approximately like the ratio of the fitted correlation lengths in the Gauss + surface to the Ginzburg-Landau model. We expect that the fluctuation observables are similarly affected by this.

D. Temperature and system-size dependence of Gaussian and non-Gaussian fluctuations

We now turn to the study of fluctuation observables in the Gauss + surface and Ginzburg-Landau models. We will concentrate on the discussion of local quantities, i.e., on the fluctuations in the net-baryon density contained within one grid spacing, on an event-by-event basis. The local variance, σ^2 , is equivalent to the equal-time correlation function $\langle(\Delta n_B)^2\rangle$ at $r = 0$. From Eq. (22), we see that $\sigma^2 \sim \xi$. Since the Gaussian mass parameter $m \sim 1/\xi$ drops rapidly around T_c with a minimum at T_c , cf. Fig. 1, we expect that the local variance is largest at T_c in both the Gauss + surface and the Ginzburg-Landau models. The local excess kurtosis, κ , is defined as

$$\kappa = \frac{\mu_4}{\sigma^4} - 3, \quad (24)$$

where $\mu_4 = \langle(\Delta n_B)^4\rangle$ at $r = 0$ is the fourth central moment of local fluctuations. The excess kurtosis must vanish for the Gaussian models while in the presence of nonlinear coupling terms it provides a measure for the non-Gaussianity of the equilibrium distribution. The local skewness was found to be subject to large statistical uncertainties in the studied finite-size systems with charge conservation and as a consequence will not be discussed in this work.

In Fig. 7, we show numerical results for the system-size dependence of σ^2 and κ in the Gauss + surface and Ginzburg-Landau models for two different T at fixed resolution $\Delta x = (20/256)$ fm. In the Gauss + surface model, the continuum expectation of σ^2 for an infinite system is given by

$$\sigma^2 = \frac{n_c^2}{2A\sqrt{Km}}, \quad (25)$$

which is indicated by the gray dotted lines. In a finite-size system, the local variance can be significantly smaller due to charge conservation, cf. Fig. 3, but increases with increasing L approaching the limit Eq. (25). The observed reduction of σ^2 in the Ginzburg-Landau model is in line with the behavior seen in m_{eff} and $\tilde{\xi}$; see Fig. 5 and the discussion in Sec. III B. We find a negligible residual Δx -dependence in σ^2 for all T and L similar to $\tilde{\xi}$. This is in contrast to the behavior noted in [64] for the pure Gaussian model where the local variance depends explicitly on the resolution, cf. Eq. (23). This unphysical behavior is cured

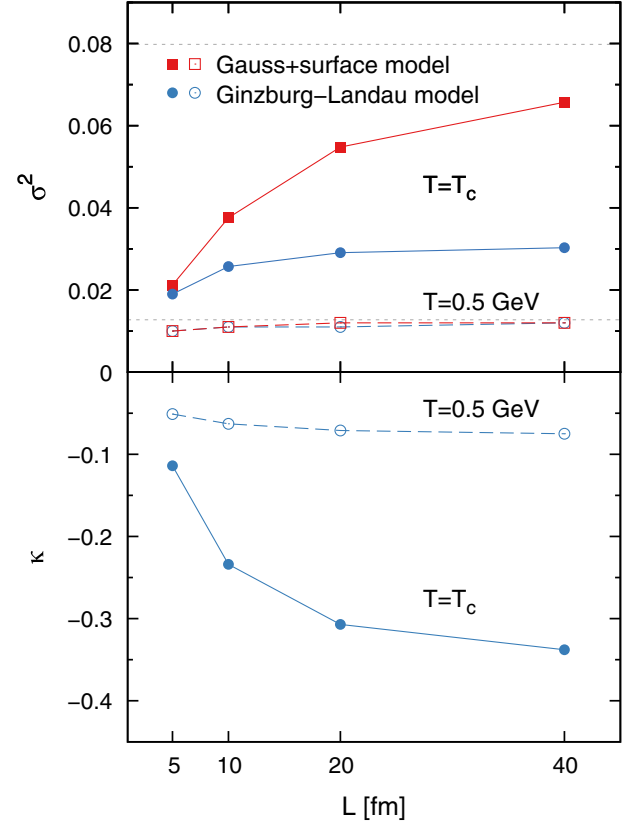


FIG. 7. Results for the local variance σ^2 and local excess kurtosis κ in the Gauss + surface (squares) and Ginzburg-Landau (circles) models for different system sizes L at fixed resolution $\Delta x = (20/256)$ fm for two different temperatures, $T = 0.5$ GeV (open symbols) and $T = T_c$ (solid symbols). The horizontal, gray dotted lines in the upper panel show for comparison the corresponding continuum expectations for σ^2 in the Gauss + surface model for an infinite system, cf. Eq. (25).

by the inclusion of a finite surface tension; see also the discussion in [68]. The local excess kurtosis vanishes within the statistical uncertainty in the Gauss + surface model. In the Ginzburg-Landau model, instead, κ is non-zero and found to increase in magnitude with L but also seems to approach a limiting value with increasing system size. The residual Δx -dependence is a bit stronger than for σ^2 but still on the few-percent level. Both σ^2 and κ are significantly larger at $T = T_c$ (solid squares and circles) than at $T = 0.5$ GeV (open squares and circles), where the influence of the Gaussian mass parameter is expected to dominate. Near T_c finite-size effects in both observables are clearly more pronounced than at $T = 0.5$ GeV and appear to be quantitatively stronger in the higher-order fluctuation observable κ .

In Fig. 8, we compare the temperature dependence of the local variance and local excess kurtosis in the Gauss + surface (squares) and Ginzburg-Landau (circles) models for $L = 20$ fm with $N_x = 256$. The reduction seen in σ^2 for the Ginzburg-Landau model compared to the Gauss + surface

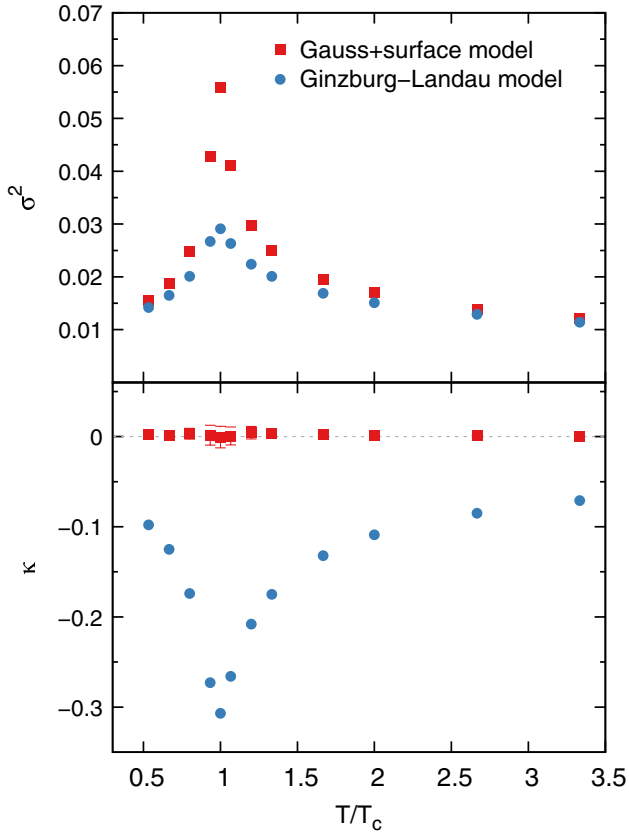


FIG. 8. Results for the local variance σ^2 and local excess kurtosis κ as functions of the scaled temperature T/T_c in the Gauss + surface (squares) and Ginzburg-Landau (circles) models for simulations with $L = 20$ fm and $\Delta x = L/256$.

model is in line with the findings for the temperature dependence of the fitted correlation length in Fig. 6. In fact, within the numerics, we find that σ^2 scales approximately as $\sigma^2 \sim \xi$ for all T as expected from Eq. (25). The numerical results for the local excess kurtosis highlight an important difference between the two models: while κ vanishes within the acquired statistics in the Gauss + surface model, it is nonzero and negative for the chosen values of $\tilde{\lambda}_i$ in the Ginzburg-Landau model. One observes a nonmonotonic temperature dependence with a prominent peak structure in the vicinity of T_c , where $\tilde{\lambda}_4$ and $\tilde{\lambda}_6$ become the dominant parameters, cf. Fig. 1.

IV. DYNAMICS OF GAUSSIAN AND NON-GAUSSIAN FLUCTUATIONS

We now turn to the study of the dynamics of the system, which we discuss in three steps: first, we investigate the dynamical properties in equilibrium in form of the dynamic structure factor, next we study the response of the system to a sudden quench in temperature, and finally look at a Hubble-like reduction of the temperature as a function of time. Note that the dynamical properties depend on the value and/or the temporal behavior of the diffusion

coefficient D , which as a function of temperature is defined as $D = \Gamma T/n_c$, where we fix $D(T_0) = 1$ fm at $T = T_0 = 0.5$ GeV unless otherwise specified.

A. Dynamic structure factor and relaxation time

The dynamical properties of the system in equilibrium at a fixed temperature are encoded in the dynamic structure factor. The time dependence of the spatial spectrum of the fluctuating net-baryon density is related to the spatial Fourier transform of the stochastic diffusion equation, Eq. (15), and can be obtained from $S(k, \omega)$ by the Fourier transformation into the time domain viz

$$\begin{aligned} S(k, t) &\equiv V \langle \Delta \hat{n}_B(k, t') \Delta \hat{n}_B^*(k, t' + t) \rangle \\ &= \frac{1}{2\pi} \int_{-\infty}^{\infty} S(k, \omega) e^{i\omega t} d\omega. \end{aligned} \quad (26)$$

For the Gaussian models with $S(k, \omega)$ given in Eq. (16), this amounts to

$$S(k, t) = S(k) \exp(-t/\tau_k) \quad (27)$$

in the continuum limit, where the static structure factor $S(k)$ is given by Eq. (18) or (19) and the inverse relaxation time reads

$$\tau_k^{-1} = \frac{Dm^2}{n_c} \left(1 + \frac{K}{m^2} k^2 \right) k^2. \quad (28)$$

By setting $K = 0$, we find the expression of τ_k for the pure Gaussian model.

Numerically, we study the dynamic structure factor $S_{k,t}$ in discretized space-time by analyzing the correlator of the density fluctuations in the mixed representation for modes with given wave vector \vec{k} and wave number $\kappa = kL/(2\pi)$; see Appendix E. Exemplarily for $\kappa = 2$, we contrast $S_{k,t}$ at $T = T_c$ for the Gauss + surface and Ginzburg-Landau models in Fig. 9. One clearly observes an exponential decay of the correlator in both models similar to the expected behavior in the continuum limit. As for the static observables, the nonlinear interactions in the Ginzburg-Landau model reduce the dynamic structure factor compared to the Gauss + surface model and, in addition, accelerate its exponential decay. We note that in the pure Gaussian model $S_{k,t}$ for the same κ is much larger and relaxes significantly slower than in the other models.

The relaxation time in the Gauss + surface model for a specific mode k can be determined by fitting the corresponding $S_{k,t}$ with an exponential ansatz of the form of the continuum expression. For $T = 0.5$ GeV and $T = T_c$, the results for not too large κ are shown in Fig. 10 (red squares). As one would expect, τ_k is drastically enhanced near T_c and long-wavelength (small κ) modes relax significantly slower than short-wave (large κ) fluctuations. The continuum results based on Eq. (28) are also shown as red solid lines

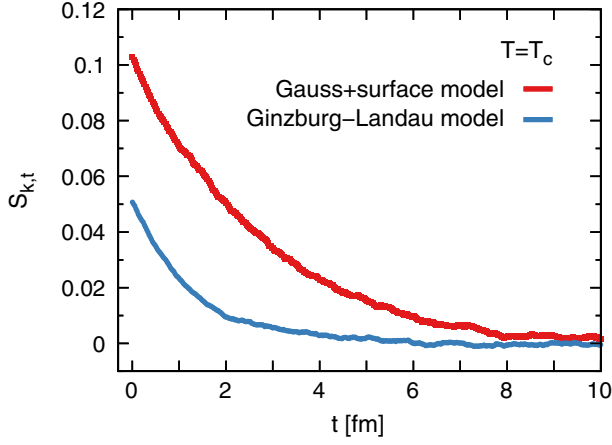


FIG. 9. The dynamic structure factor $S_{k,t}$ as a function of time for $\kappa = 2$ in the Gauss + surface and Ginzburg-Landau models for $L = 20$ fm and $N_x = 256$ at $T = T_c$.

in Fig. 10. We find that the results of the fits to the data from simulations with $\Delta x = (20/256)$ fm are already very close to the continuum expectations for not too large κ (see the discussion in Appendix E).

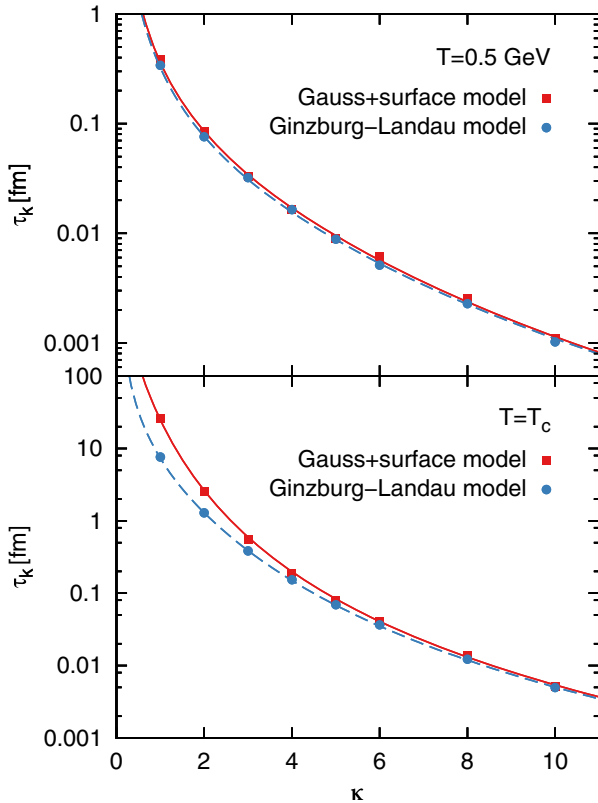


FIG. 10. Relaxation time τ_k (symbols) as a function of κ for $L = 20$ fm and $N_x = 256$ at $T = 0.5$ GeV (upper panel) and $T = T_c$ (lower panel) in the Gauss + surface and Ginzburg-Landau models. The results are compared with the continuum expression of the Gauss + surface model, Eq. (28), shown as red solid lines, and a modified expression with m replaced by m_{eff} , see Fig. 4, shown as blue dashed lines.

The exponential decay of $S_{k,t}$ seen in Fig. 9 for the Ginzburg-Landau model suggests to use a similar ansatz to determine τ_k in this case. The results are shown by blue circles in Fig. 10. The nonlinear interactions are found to reduce the fitted relaxation time, in particular, for modes with small κ , and the effect is more prominent in the vicinity of T_c . For larger κ , fluctuations are less affected by the nonlinear interactions and τ_k in the Gauss + surface and the Ginzburg-Landau model is comparable. The k -dependence of our numerical results for τ_k in the Ginzburg-Landau model can quite accurately be described by the continuum expression Eq. (28) of the Gauss + surface model by replacing m with m_{eff} ; see blue dashed lines in Fig. 10. The values for the modified Gaussian mass parameter $m_{\text{eff}} > m$ are those necessary for describing the behavior of the static structure factor in the Ginzburg-Landau model discussed in Sec. III B.

The comparison of the fit results with the analytic expectations in the Gauss + surface model indicates that the simulations carried out with $N_x = 256$ at $L = 20$ fm

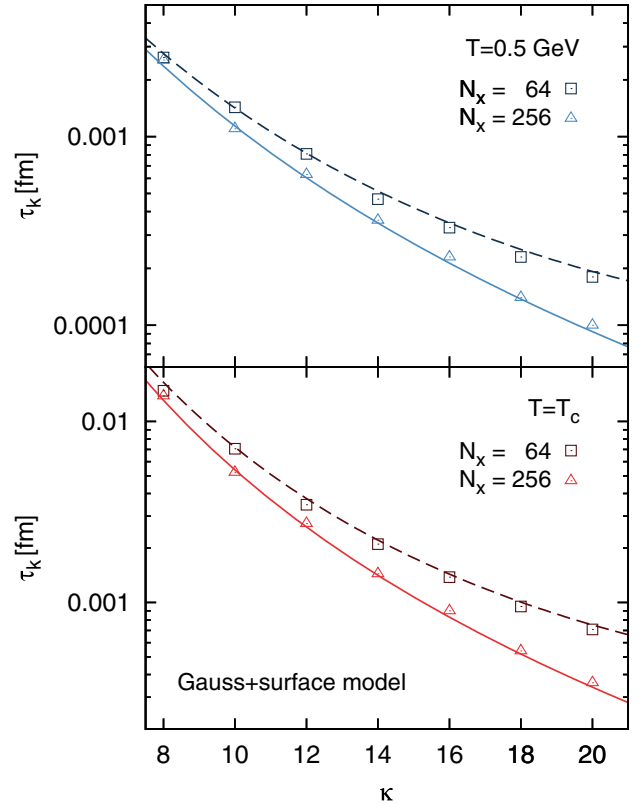


FIG. 11. Dependence of the relaxation time (symbols) on the resolution in the Gauss + surface model ($\lambda_3 = \lambda_4 = \lambda_6 = 0$). We contrast for $T = 0.5$ GeV (upper panel) and $T = T_c$ (lower panel) simulations for $N_x = 64$ (squares) and $N_x = 256$ (triangles) at fixed $L = 20$ fm. Analytic expectations based on Eqs. (E9)–(E11) are shown as dashed and solid lines, respectively. We note that the analytic results based on Eq. (28) and on Eqs. (E9)–(E11) are practically indistinguishable for $\Delta x = (20/256)$ fm in the shown range of κ .

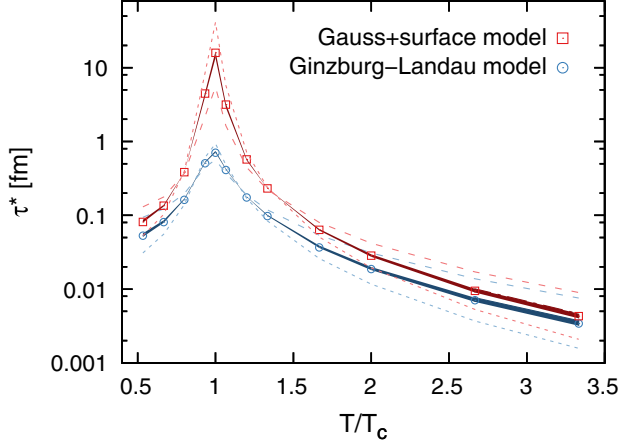


FIG. 12. Scaling behavior of the relaxation time τ^* for modes with $k^* = 1/\tilde{\xi}$ with the correlation length $\tilde{\xi}$ in Gauss + surface and Ginzburg-Landau models as a function of T/T_c . Fit results to simulations with $L = 20$ fm and $N_x = 256$ (symbols) are contrasted with the scaling ansatz $a\tilde{\xi}^z$, where $a \simeq 0.08/(D \text{ fm}^{z-2})$ and $z = 4 \pm 0.1$ (filled bands) give the best fit, and $z = 3$ (dashed lines) and $z = 5$ (dotted lines) are also indicated.

are already sufficiently close to the continuum limit, also for the dynamic observables. To test further how well analytic expectations for resolution effects are reproduced numerically, we decrease the resolution in the simulations by a factor 4 and consider $N_x = 64$. From Eqs. (E9)–(E11), one expects that a decrease in resolution results in an increase of the fitted relaxation time, in particular for larger κ . This is precisely observed in the results depicted in Fig. 11. In fact, the comparison of the fit results for τ_k with the expectations for the relaxation time, Eqs. (E9)–(E11), shows that resolution effects are well controlled.

The determination of the dynamic structure factor and of the relaxation time allows us to study the correlation length dependence of τ_k for modes which are correlated over the distance $\tilde{\xi}$. For this purpose, we analyze τ^* , the relaxation time of modes with $k^* = 1/\tilde{\xi}(T)$, as a function of T , where $\tilde{\xi}(T)$ is the fitted correlation length discussed in Sec. III C. Results for the Gauss + surface and Ginzburg-Landau models are shown in Fig. 12 (symbols). We find τ^* to behave like $a\tilde{\xi}^z$ with proportionality factor a and dynamic scaling (critical) exponent z . For both models, the best fit (filled bands in Fig. 12) gives $z = 4 \pm 0.1$ and $a \simeq 0.08/(D \text{ fm}^{z-2})$. This proportionality factor confirms our expectations, $a = n_c \xi_0 / (D(1 + \tilde{K}))$, based on the continuum expression of τ_k in the Gauss + surface model. We also indicate that other scaling exponents, e.g., $z = 3$ (dashed lines) or $z = 5$ (dotted lines), fail to describe the numerically realized scaling with the correlation length. This shows that our simulations reproduce the dynamic scaling behavior one would expect for the stochastic diffusion of a conserved charge which is one of the models B within the classification scheme [9].

B. Relaxation of fluctuation observables after a temperature-quench

The relaxation dynamics of fluctuation observables such as the local variance σ^2 and the local excess kurtosis κ toward equilibrium can be studied through the sudden quench in temperature from a well-prepared initial condition. For this purpose, we first let the system equilibrate at $T = T_0 = 0.5$ GeV and then instantaneously reduce the temperature at time $\tau = \tau_0$ to three distinct values T^* , namely, $T^* = T_c$, $T^* = 0.18$ GeV, and $T^* = 0.2$ GeV. We discuss these three quench scenarios only for the Ginzburg-Landau model. Qualitatively, the same conclusions can be drawn for σ^2 in the Gauss + surface model.

The results for the relaxation behavior of σ^2 and κ are shown in Fig. 13. One observes that the relaxation dynamics is quite abrupt initially. We find that with decreasing quench-temperature T^* the time it takes σ^2 and κ to relax to the corresponding equilibrium result (horizontal, gray dotted lines) increases. This is to be expected since for smaller T^* we have a smaller diffusion coefficient D and, moreover, the difference between the equilibrium values at T_0 and at a T^* close to T_c is larger. In addition, higher

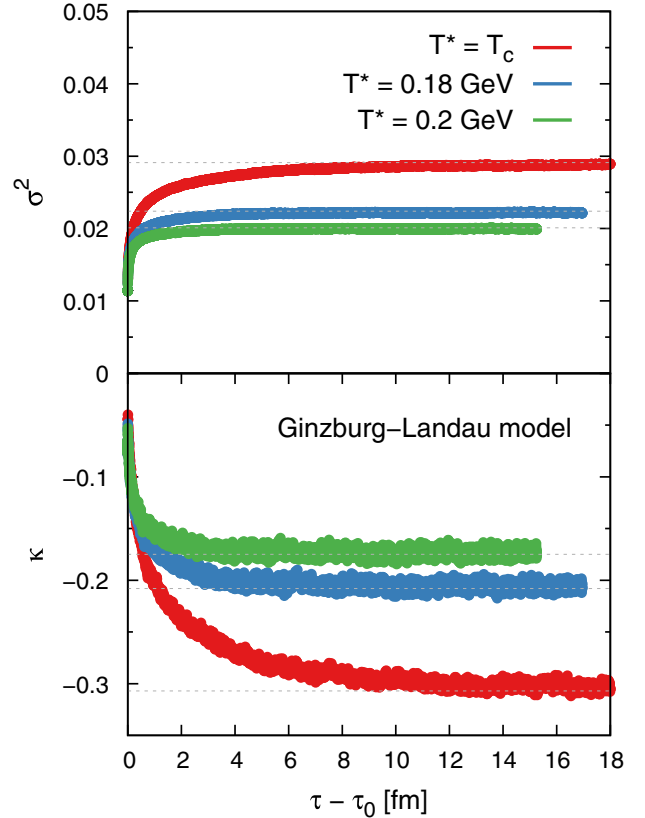


FIG. 13. Relaxation dynamics of the local variance σ^2 and the local excess kurtosis κ toward their equilibrium values under a sudden quench in temperature from equilibrium at $T_0 = 0.5$ GeV to T^* at time $\tau = \tau_0$. The shown results are for the Ginzburg-Landau model with $L = 20$ fm and $N_x = 256$.

moments appear to approach their equilibrium expectations slower. By increasing the initial value of the diffusion coefficient to $D(T = T_0) = 2$ fm, the relaxation rate is overall increased and the fluctuation observables relax quicker toward equilibrium; see also the discussions in [64,68]. We note that the determination of the relaxation time of fluctuation observables within a quench scenario can allow the identification of structures in the QCD phase diagram. This was demonstrated in a QCD-assisted transport approach based on nonequilibrium chiral fluid dynamics and the effective action of low-energy QCD in [66].

C. Time evolution of fluctuations in a cooling system

Assuming a dynamical evolution of the temperature of the system allows us to highlight some important non-equilibrium effects. For this purpose, we consider a simple, spatially homogeneous time dependence of T in the Hubble-like form

$$T(\tau) = T_0 \left(\frac{\tau_0}{\tau} \right)^{dc_s^2}, \quad (29)$$

with dimension $d = 3$, speed of sound $c_s^2 = 1/3$ and $T_0 = 0.5$ GeV at initial time $\tau_0 = 1$ fm at which the system is in equilibrium. For this cooling scenario, the critical temperature is reached at $\tau_c - \tau_0 = 2.33$ fm. The time-dependent temperature translates into time-dependent couplings via Eqs. (10)–(14), which are shown in Fig. 14. Due to the fast initial decrease of T and the slower decrease at later times in Eq. (29), the thermodynamic correlation length is more symmetric between the early and late times than it is in comparison to the high and low temperatures in Fig. 1. Still,

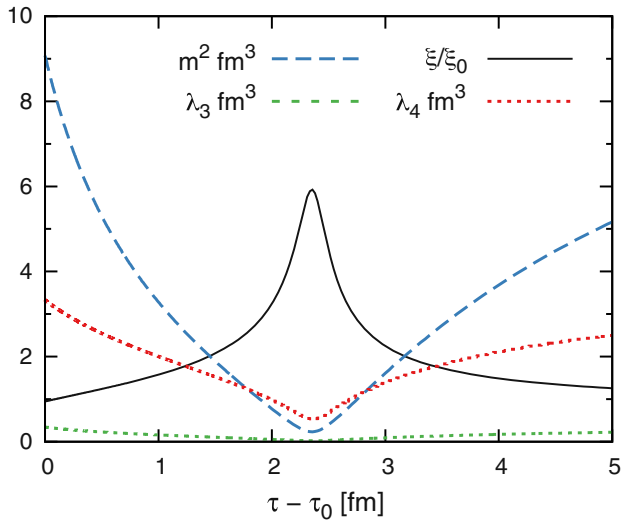


FIG. 14. Time dependence of the parameters entering the Ginzburg-Landau free energy functional \mathcal{F} in Eq. (9); see Fig. 1 for comparison. The coupling $\lambda_6 = 1/\text{fm}^3$ (not shown) is set constant. The critical temperature $T_c = 0.15$ GeV is reached at $\tau_c - \tau_0 = 2.33$ fm.

all couplings except λ_6 , which is independent of the correlation length, have a dip at the time when the critical temperature is reached. This is the region where we expect nonequilibrium effects to be most prominent.

We first study the impact of the dynamical evolution of T on the equal-time correlation function and the associated correlation length $\tilde{\xi}$. The results presented here are obtained for the Ginzburg-Landau model where we analyzed a sufficient amount of events. The form of the equal-time correlation function is clearly affected by the dynamics; see upper panel in Fig. 15 (squares) for $T = T_c$. On the quantitative level, this is also determined by the temporal evolution of the diffusion coefficient D . For not too large initial values (such as $D(T_0) = 1$ fm), it already significantly decreased (to $D(T_c) = 0.3$ fm in this case) by the

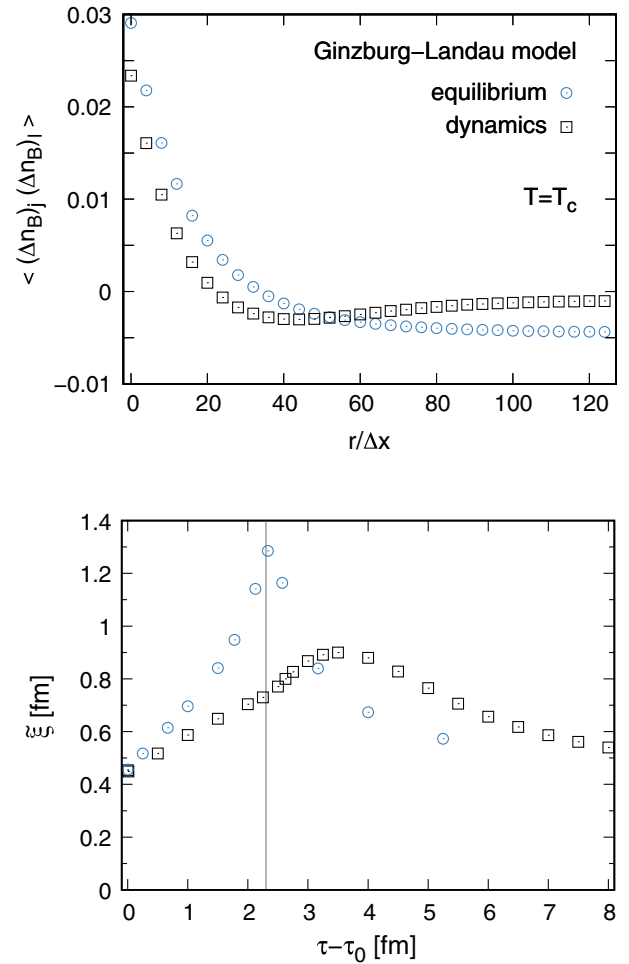


FIG. 15. Dynamical behavior (squares) of the equal-time correlation function (upper panel) and the fitted correlation length (lower panel) in a cooling system, cf. Eq. (29), in comparison with the equilibrium situation (circles) at the same T . The results are obtained for the Ginzburg-Landau model with $L = 20$ fm and $N_x = 256$. We show a snapshot of the correlation function as a function of distance $r = |j - l|\Delta x$ with $\Delta x = L/N_x$ at time $\tau_c - \tau_0 = 2.33$ fm, i.e., at $T = T_c$, and $\tilde{\xi}$ as a function of $\tau - \tau_0$, where the vertical line indicates $\tau_c - \tau_0$.

time T_c is reached and, thus, local fluctuations cannot rapidly enough be balanced throughout the entire finite-size system. As a consequence, correlations at zero distance do not build up quickly enough from the smaller value at T_0 toward the equilibrium value at T_c [see the upper panel in Fig. 15 (circles) and Fig. 8] and lag behind. Around these local fluctuations, anticorrelations are present due to charge conservation. In the dynamical situation, they do not have sufficient time to diffuse into the entire system. We therefore see a dip of the correlation function around $r = 40 \Delta x$, while it approaches zero at larger distances. This local balancing of the fluctuations reduces the correlation length, as we discuss in the following.

While the form of the equal-time correlation function in the dynamical scenario is not in one-to-one correspondence with the equilibrium form, we may still analyze the visible exponential decrease in the region from small to intermediate distances to deduce a correlation length. By using the ansatz employed in Sec. III C for different T , i.e., at different times $\tau - \tau_0$, we obtain the result for the dynamical $\tilde{\xi}$ shown in the lower panel of Fig. 15 (squares). In comparison to the equilibrium result (circles, cf. also Fig. 6), we observe clear deviations highlighting two distinct nonequilibrium effects: first, the overall magnitude of $\tilde{\xi}$ is significantly reduced as a consequence of the dynamics. Second, there are clear indications for a retardation effect due to the rapid cooling in T . The dynamical $\tilde{\xi}$ remains initially smaller than its equilibrium counterpart for given T but then develops a maximum at a temperature far below T_c such that at late times it is actually larger than in the equilibrium situation. The pronounced structure traditionally associated with the phase transition is shifted to later times and, thus, different thermal conditions. We expect similar effects for the fluctuation observables.

In Fig. 16, we show the temporal evolution of the local variance σ^2 (upper panel) and the local excess kurtosis κ (lower panel) as a function of time in the Gauss + surface (red bands) and Ginzburg-Landau (blue bands) models. For both models, σ^2 peaks at a time $\tau - \tau_0$ shortly after T_c is reached during the evolution. The retardation shift appears slightly larger in the Gauss + surface than in the Ginzburg-Landau model. As in the equilibrium situation, σ^2 in the Ginzburg-Landau model stays below the Gauss + surface model result, but the reduction of its maximal value due to the dynamics is significantly stronger in the Gauss + surface model (by 46% compared to 17% for the Ginzburg-Landau model).

For the local excess kurtosis, we note that in the absence of nonlinear coupling terms κ vanishes in the dynamical scenario as it did in equilibrium (see red band and open squares in the lower panel of Fig. 16). For the Ginzburg-Landau model, κ starts at its equilibrium value for T_0 and initially follows the equilibrium behavior for given T (see blue band and open circles in the lower panel of Fig. 16). However, within the band of statistical uncertainties, it

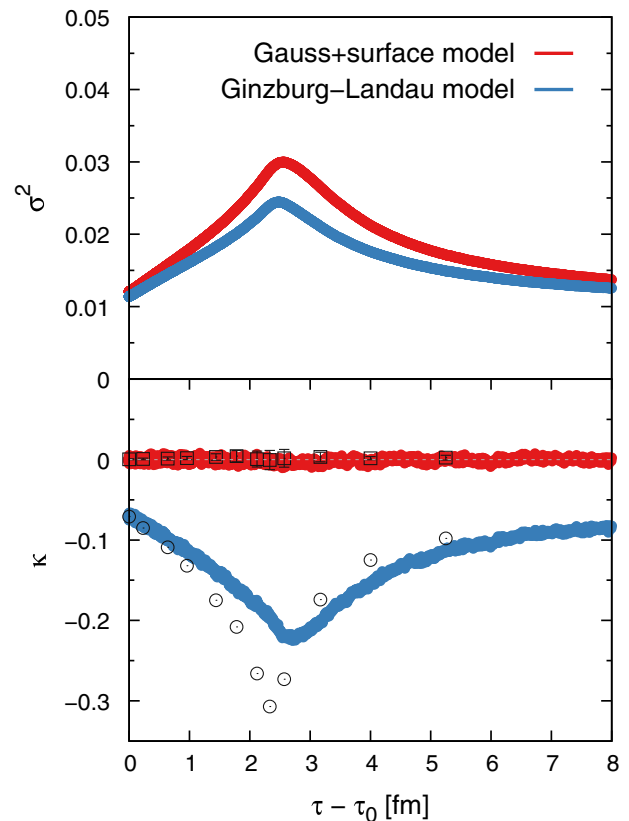


FIG. 16. Dynamical behavior (colored bands) of the local variance σ^2 and the local excess kurtosis κ for the Gauss + surface and Ginzburg-Landau models in a cooling system, cf. Eq. (29), as a function of time. For the local excess kurtosis, we compare with the equilibrium results (open squares and circles) at the corresponding T . The shown results are for $L = 20$ fm and $N_x = 256$.

quickly lags behind the equilibrium situation as reflected in the reduced magnitude of κ . We can clearly see that in the dynamical scenario the minimum in the local excess kurtosis is shifted to a later time than $\tau_c - \tau_0$ and that the magnitude of this minimum is significantly reduced (by approximately 30%) compared to the equilibrium result. At later times, the retardation effect leads to a dynamical κ slightly larger in magnitude than in equilibrium. As is evident from Fig. 16, the nonequilibrium effects influence κ stronger than σ^2 in the Ginzburg-Landau model. The behavior seen in the fluctuation observables resembles qualitatively the one discussed for $\tilde{\xi}$ above with an important difference: the shift of the maximum in $\tilde{\xi}$ to smaller T is larger than in σ^2 or κ . In future work, we will investigate the fluctuation observables over larger subvolumes to see if the relation with the correlation length is restored. We note that an overall reduction of the dynamical diffusion coefficient (by lowering its initial value $D(T_0)$) results in a stronger retardation and a stronger reduction of the magnitude of the fluctuation signal.

V. DISCUSSION

In this work, we presented a first rigorous implementation of the one-dimensional stochastic diffusion equation near the QCD critical point. First, we benchmarked this implementation in the linear approximation, including Gaussian mass and surface tension terms, versus analytic results of the equal-time correlation function and the static structure factor. Based on these tests, we chose the resolution of the spatial discretization as to reproduce the behavior of the first 50% of the wave numbers in the continuum limit. Charge conservation is found to play an important role for the correlation function and limits the growth of long-range correlations. In the same sense, the growth of the correlation length near T_c is limited for system sizes up to a few times the thermodynamic correlation length.

In equilibrium, we investigated the temperature dependence of the local variance and excess kurtosis. The latter takes nonzero values as soon as the nonlinear coupling terms in the Ginzburg-Landau free energy functional are included. The expected nonmonotonic behavior around T_c is clearly observed. The inclusion of the nonlinear coupling terms reduces the variance of the system by a factor of 2 near T_c .

From the dynamic structure factor, we obtained the relaxation time of the critical mode. It is found to scale with the correlation length according to model B of dynamical universality. Finally, we investigated the response of the system to changes of the temperature, first, via a sudden quench in temperature and, second, via a Hubble-like time evolution. We observe again that the growth of the correlation length is limited by charge-conservation effects, this time in a dynamical setup. Here, fluctuations do not have enough time to diffuse to larger distances and, thus, the correlation length is limited to a smaller range. Fluctuation observables are reduced in magnitude and shifted to smaller temperatures due to nonequilibrium effects. Higher-order cumulants are impacted stronger than the variance by the nonequilibrium situation, i.e., they need more time to relax, the magnitude of their extrema is more reduced compared to the equilibrium values and the retardation effect is stronger.

We emphasize in particular the importance of benchmarking the approach to the dynamics of fluctuations against analytic results, like the correlation function, the static and the dynamic structure factor. This should be a standard requirement for all models dealing with the dynamics of fluctuations, including more complex approaches to fluctuating fluid dynamics.

The presented cumulants are evaluated as local observables over individual cells of the simulation region, which serves well the purpose of understanding the basic dynamics of fluctuations in stochastic partial differential equations. For aiming at a comparison with experimental data from heavy-ion collisions, integrated observables in finite kinematic regions are of additional interest. A study of fluctuations over larger subregions of observation similar

to [65] and of their systematics will address these questions and be reported elsewhere. In our studies of the time evolution of the temperature, the considered systems did not expand. We plan to investigate the expansion of the system in a next step, see [91], to include regular contributions into the free energy functional and to extend the treatment of fluctuations to three spatial dimensions.

ACKNOWLEDGMENTS

The authors acknowledge the support of the program ‘‘Etoiles montantes en Pays de la Loire 2017.’’ This research was supported in part by the ExtreMe Matter Institute at the GSI Helmholtzzentrum für Schwerionenforschung, Darmstadt, Germany. The authors thank S. A. Bass and T. Schäfer for stimulating discussions.

APPENDIX A: NUMERICAL IMPLEMENTATION

We study the stochastic diffusion Eq. (15) by discretizing the diffusive net-baryon density on N_x sites equally distributed over a system of longitudinal extent L with resolution (grid spacing) $\Delta x = L/N_x$. Over the finite Δx of a cell, n_B must be understood as being averaged. Time is discretized in steps of Δt at which n_B is considered pointwise. Details about the extent and discretization in the transverse direction are not important as we study the evolution of the system and physical observables only in the longitudinal direction which is decoupled from the transverse dynamics. For simplicity, we set the transverse area $A = 1 \text{ fm}^2$ but have verified the proper behavior with A in the numerics. The Gaussian white noise must be understood as averaged over space Δx and time Δt . It is independent between different cells and time steps with zero mean and variance $1/(\Delta x \Delta t)$.

Equation (15) is solved by means of a semi-implicit scheme. While the operator associated with the Gaussian mass and surface tension terms is treated implicitly in time, the operator associated with the nonlinear coupling terms is discretized explicitly. The temporal integration is performed with a predictor-corrector method. For the stochastic diffusion equation of the general form

$$\frac{dn_B}{dt} = \mathcal{O}_l n_B + \mathcal{O}_{nl}(n_B) + \mathcal{O}_\xi W, \quad (\text{A1})$$

this amounts to solving in a first step

$$\left(1 - \frac{\Delta t}{2} \mathcal{O}_l\right) \tilde{n}_B^{m+1} = \left(1 + \frac{\Delta t}{2} \mathcal{O}_l\right) n_B^m + \Delta t \mathcal{O}_{nl}(n_B^m) + \Delta t \mathcal{O}_\xi W^m \quad (\text{A2})$$

for \tilde{n}_B^{m+1} as an intermediate update of n_B^m from time step m , and then by using n_B^m and \tilde{n}_B^{m+1} in

$$\begin{aligned} \left(1 - \frac{\Delta t}{2} \mathcal{O}_l\right) n_B^{m+1} &= \left(1 + \frac{\Delta t}{2} \mathcal{O}_l\right) n_B^m \\ &+ \frac{\Delta t}{2} [\mathcal{O}_{nl}(\tilde{n}_B^m) + \mathcal{O}_{nl}(n_B^m)] \\ &+ \Delta t \mathcal{O}_\xi W^m, \end{aligned} \quad (\text{A3})$$

one finds n_B^{m+1} as the update at time step $m+1$. The individual operators in the above equations read (we drop the index B in the following to improve readability)

$$\mathcal{O}_l n^m = \frac{D}{\Delta x^2} \frac{m^2}{n_c} (n_{j+1}^m - 2n_j^m + n_{j-1}^m) \quad (\text{A4})$$

$$\begin{aligned} -\frac{D}{\Delta x^4} \frac{K}{n_c} (n_{j+2}^m - 4n_{j+1}^m + 6n_j^m - 4n_{j-1}^m + n_{j-2}^m), \\ \mathcal{O}_{nl}(n^m) = \frac{D}{\Delta x^2} \sum_{i=3,4,6} \frac{\lambda_i}{n_c^{i-1}} [(\Delta n_{j+1}^m)^{i-1} \\ - 2(\Delta n_j^m)^{i-1} + (\Delta n_{j-1}^m)^{i-1}], \end{aligned} \quad (\text{A5})$$

$$\mathcal{O}_\xi W^m = \sqrt{\frac{2Dn_c}{A\Delta x\Delta t}} \frac{1}{\Delta x} \left(W_{j+\frac{1}{2}}^m - W_{j-\frac{1}{2}}^m \right). \quad (\text{A6})$$

This system of equations is solved for each spatial point j on the grid. The contributions from the nonlinear coupling terms are simulated by computing the corresponding power of $\Delta n_j^m = n_j^m - n_c$ at a given site j for each time step m . Without nonlinear coupling terms, the predictor and corrector steps are identical and yield exactly the same solution which makes one of the steps redundant. The noise field W in Eq. (A6) has zero mean and variance 1.

APPENDIX B: STATIC STRUCTURE FACTOR IN DISCRETIZED SPACE-TIME

For the Gauss and Gauss + surface models, for which the contributions from the nonlinear operator in Eq. (A5) vanish, analytic results for the static structure factor S_k in discretized space-time can be derived. In this limit, the general form of the stochastic diffusion equation may be written in mixed Fourier space as

$$M_k^{(1)} \hat{n}_k^{m+1} = M_k^{(-1)} \hat{n}_k^m + N_k \hat{W}_k^m, \quad (\text{B1})$$

with

$$\begin{aligned} M_k^{(a)} = 1 - a \frac{\Delta t}{2} \left(\frac{D}{\Delta x^2} \frac{m^2}{n_c} [2 \cos(\Delta k) - 2] \right. \\ \left. - \frac{D}{\Delta x^4} \frac{K}{n_c} [2 \cos(2\Delta k) - 8 \cos(\Delta k) + 6] \right), \end{aligned} \quad (\text{B2})$$

$$N_k = \sqrt{\frac{8Dn_c\Delta t}{A\Delta x^3}} \sin(\Delta k/2), \quad (\text{B3})$$

$\Delta k = k\Delta x$ and $\langle \hat{W}_k^m (\hat{W}_k^m)^* \rangle = 1/N_x$. We note that based on Eq. (15) we find that Eq. (B1) holds true also for the difference $\Delta \hat{n}_k$ instead of \hat{n}_k . From the definition

$$S_k^m = V \langle \Delta \hat{n}_k^m (\Delta \hat{n}_k^m)^* \rangle \quad (\text{B4})$$

and the condition of stationarity $S_k = S_k^m = S_k^{m+1}$ in equilibrium, one finds

$$S_k = \frac{|N_k|^2 A \Delta x}{|M_k^{(1)}|^2 - |M_k^{(-1)}|^2} \quad (\text{B5})$$

$$= \frac{n_c^2}{m^2} \frac{1}{1 + \frac{2K}{m^2 \Delta x^2} [1 - \cos(\Delta k)]} \quad (\text{B6})$$

for the static structure factor; see Eq. (20). This result is independent of the time step Δt . In the limit of the pure Gaussian model with $K = 0$, this reduces to $S_k = n_c^2/m^2$, which is independent of k and Δx and agrees with the result in the continuum; see Eq. (18). We note that for $k = 0$ the static structure factor reflects charge conservation in the entire system.

APPENDIX C: NET-BARYON NUMBER CONSERVATION IN FINITE-SIZE SYSTEMS

The net-baryon number of the entire system is numerically conserved by imposing periodic boundary conditions on the net-baryon number density. As a result, charge conservation must be reflected in the behavior of observables such as the equal-time correlation function. The latter is connected with the static structure factor by a Fourier transformation. In discretized space, one defines

$$n_j = \sum_k \hat{n}_k e^{ijk\Delta x}, \quad (\text{C1})$$

where $k = 2\pi\kappa/L$ is restricted by $0 \leq \kappa < N_x$ for $\kappa \in \mathcal{Z}$. Accordingly, the equal-time correlation function follows in discretized space as

$$\langle (\Delta n_B)_j (\Delta n_B)_l \rangle = \frac{1}{V} \sum_{\kappa=0}^{N_x-1} e^{i2\pi\kappa|j-l|/N_x} S_\kappa. \quad (\text{C2})$$

This definition holds for an infinite system. For the pure Gaussian model with $S_k = n_c^2/m^2$, one finds

$$\langle (\Delta n_B)_j (\Delta n_B)_l \rangle = \frac{n_c^2}{Am^2} \frac{\delta_{jl}}{\Delta x} \quad (\text{C3})$$

because modes with different κ are orthogonal.

For a finite-size system, however, charge conservation must be imposed by demanding that local fluctuations vanish upon summation over the entire system, i.e., $\sum_l \langle (\Delta n_B)_j (\Delta n_B)_l \rangle = 0$ for any j . This is respected if we impose

$$\begin{aligned} \langle (\Delta n_B)_j (\Delta n_B)_l \rangle &= \frac{1}{V} \sum_{\kappa=0}^{N_x-1} e^{i2\pi\kappa|j-l|/N_x} S_\kappa \\ &\quad - \frac{1}{N_x V} \sum_{h=0}^{N_x-1} \sum_{\kappa=0}^{N_x-1} e^{i2\pi\kappa h/N_x} S_\kappa. \end{aligned} \quad (\text{C4})$$

Instead of Eq. (C3), one finds

$$\langle (\Delta n_B)_j (\Delta n_B)_l \rangle = \frac{n_c^2}{Am^2} \left(\frac{\delta_{jl}}{\Delta x} - \frac{1}{L} \right) \quad (\text{C5})$$

for the pure Gaussian model. The finite-size correction vanishes in the thermodynamic limit for any given resolution Δx .

For the Gauss + surface model with S_κ given in Eq. (B5), the result of the summations in Eq. (C4) can be obtained numerically. Due to Eq. (C4), one expects a negative shift in a finite-size system. This shift has to become less pronounced with increasing N_x , i.e., for fixed resolution Δx with increasing L . Both these features are seen in the numerics, cf. Fig. 3.

APPENDIX D: DETERMINATION OF THE CORRELATION LENGTH

The form of the equal-time correlation function found in the equilibrium simulations is that of an exponential decay which is modified by a negative shift due to exact charge conservation. Since in equilibrium the system is homogeneous on length scales larger than the noise correlation, this shift is expected to be a constant. Then, a suitable ansatz to determine the correlation length $\tilde{\xi}$ is

$$\langle (\Delta n_B)_j (\Delta n_B)_l \rangle = \frac{C_1}{C_2} \exp(-|j-l|\Delta x/C_2) + C_3, \quad (\text{D1})$$

where C_2 is the fit parameter for $\tilde{\xi}$ in dependence of Δx , L , and T . The quantity $C_1/C_2 + C_3$ gives the value of the correlation function over distances of the grid spacing Δx , i.e., the value of the local variance. The fit results for $\tilde{\xi}$ shown in Sec. III C are obtained by optimizing the description of the local variance in the numerics. We observe that for the Gauss + surface model simulations with $L = 20$ fm the obtained value of C_1/C_2 is already quite close to the continuum expectation of $n_c^2/(2Am\sqrt{K})$ for the local variance in an infinite system, cf. Eqs. (22) and (25), even for T near T_c . We note that for smaller L this is not necessarily the case, in particular close to T_c . Motivated by the fact that the equilibrium results of the equal-time correlation function in the Ginzburg-Landau model can be described by the theoretical expectation of the Gauss + surface model with a modified, effective Gaussian mass parameter, see Sec. III B, we utilize the same ansatz Eq. (D1) and strategy in order to fit the numerical results of the Ginzburg-Landau model and to determine $\tilde{\xi}$.

APPENDIX E: DYNAMIC STRUCTURE FACTOR IN DISCRETIZED SPACE-TIME

The diffusion equation in discretized space-time discussed in Appendix A has for the Gauss and Gauss + surface models the following representation in full (ω, k) Fourier-space:

$$M_k^{(1)} e^{i\Delta\omega} \hat{n}_{k,\omega} = M_k^{(-1)} \hat{n}_{k,\omega} + N_k \hat{W}_{k,\omega}, \quad (\text{E1})$$

with $\Delta\omega = \omega\Delta t$. This implies for the correlator

$$\begin{aligned} \langle \Delta \hat{n}_{k,\omega} \Delta \hat{n}_{k,\omega}^* \rangle &= \frac{N_k \langle \hat{W}_{k,\omega} \hat{W}_{k,\omega}^* \rangle N_k^*}{(M_k^{(1)} - e^{-i\Delta\omega} M_k^{(-1)}) (M_k^{(1)*} - e^{i\Delta\omega} M_k^{(-1)*})}, \end{aligned} \quad (\text{E2})$$

which gives the dynamic structure factor via

$$S_{k,\omega} = \lim_{N_t \rightarrow \infty} V(N_t \Delta t) \langle \Delta \hat{n}_{k,\omega} \Delta \hat{n}_{k,\omega}^* \rangle, \quad (\text{E3})$$

where N_t is the number of (performed) time steps. From this definition, it is clear that the dynamic structure factor is a late-time equilibrium observable. For white noise, we have $\langle \hat{W}_{k,\omega} \hat{W}_{k,\omega}^* \rangle = 1/(N_x N_t)$, and with $M_k^{(a)}$ and N_k defined in Appendix B we obtain

$$S_{k,\omega} = \frac{2n_c^3 \tilde{\chi}_1 D k^2}{n_c^2 \Delta t^{-2} (1 - \cos(\Delta\omega)) + \tilde{\chi}_2 \tilde{\chi}_1^2 D^2 k^4}, \quad (\text{E4})$$

with

$$\tilde{\chi}_1 = (1 - \cos(\Delta k))/\Delta k^2, \quad (\text{E5})$$

$$\tilde{\chi}_2 = m^4 \left(1 - \frac{2K}{m^2 \Delta x^2} (\cos(\Delta k) - 1) \right)^2 (1 + \cos(\Delta\omega)). \quad (\text{E6})$$

The result for the pure Gaussian model is found by setting $K = 0$ in Eq. (E6). In the limit of small $\Delta\omega \ll 1$, we can expand $\cos(\Delta\omega)$ and find

$$\begin{aligned} \lim_{\Delta\omega \ll 1} S_{k,\omega} &= \frac{4n_c \tilde{\chi}_1 D k^2}{\omega^2 + 4D^2 \frac{m^4}{n_c^2} k^4 \tilde{\chi}_1^2 \left(1 - \frac{2K}{m^2 \Delta x^2} (\cos(\Delta k) - 1) \right)^2}. \end{aligned} \quad (\text{E7})$$

Moreover, in the limit of small $\Delta k \ll 1$, we have $\tilde{\chi}_1 \approx \frac{1}{2} - \frac{1}{24} \Delta k^2$ and $(2 \cos(\Delta k) - 2)/\Delta x^2 \approx -k^2 + \frac{1}{12} k^2 \Delta k^2$ in Eq. (E7). Thus, for given ω and k , in the limit of $\Delta t \rightarrow 0$ and $\Delta x \rightarrow 0$, the continuum expression Eq. (16) of the dynamic structure factor $S(k, \omega)$ is recovered from $S_{k,\omega}$. In the numerics, finite resolution in Δt and Δx implies deviations from the continuum result. Therefore, only the

regime of small wave vectors and low frequencies allow us to judge the accuracy of the numerical scheme. Even in the limit $\Delta t \rightarrow 0$, the approach to the continuum is limited to small values of k depending on the spatial resolution. This limit can be used to determine an analytic expression for the dynamic structure factor $S_{k,t}$ in the mixed representation from the Fourier transformation into the time-domain. We find

$$S_{k,t} = \frac{1}{2\pi} \int_{-\infty}^{\infty} e^{i\omega t} \lim_{\Delta t \rightarrow 0} S_{k,\omega} d\omega = S_k e^{-t/\tau_k}, \quad (\text{E8})$$

where S_k is the static structure factor in Eq. (B5) and τ_k is the relaxation time of fluctuations with wave vector $k = 2\pi\kappa/L$ given via

$$\tau_k^{-1} = 2 \frac{D}{n_c} m^2 k^2 (A_k + B_k), \quad (\text{E9})$$

with

$$A_k = (1 - \cos(\Delta k))/\Delta k^2, \quad (\text{E10})$$

$$B_k = \frac{2Kk^2(1 - \cos(\Delta k))^2}{m^2 \Delta k^4}. \quad (\text{E11})$$

From Eqs. (E9)–(E11) in the limit of small Δx , we see that finite-resolution effects increase τ_k compared to the continuum result Eq. (28), which is approached in the limit $\Delta x \rightarrow 0$. Moreover, we find that τ_k is smaller in the Gauss + surface model compared to the pure Gaussian model with $K = 0$. This effect is less pronounced for small values of κ and away from the transition temperature T_c .

-
- [1] T. Schäfer, Fluid dynamics and viscosity in strongly correlated fluids, *Annu. Rev. Nucl. Part. Sci.* **64**, 125 (2014).
 - [2] P. Kovtun, Lectures on hydrodynamic fluctuations in relativistic theories, *J. Phys. A* **45**, 473001 (2012).
 - [3] S. Jeon and U. Heinz, Introduction to hydrodynamics, *Int. J. Mod. Phys. E* **24**, 1530010 (2015).
 - [4] P. Kovtun and L. G. Yaffe, Hydrodynamic fluctuations, long time tails, and supersymmetry, *Phys. Rev. D* **68**, 025007 (2003).
 - [5] Y. Akamatsu, A. Mazeliauskas, and D. Teaney, A kinetic regime of hydrodynamic fluctuations and long time tails for a Bjorken expansion, *Phys. Rev. C* **95**, 014909 (2017).
 - [6] M. Martinez and T. Schäfer, Stochastic hydrodynamics and long time tails of an expanding conformal charged fluid, *Phys. Rev. C* **99**, 054902 (2019).
 - [7] X. An, G. Basar, M. Stephanov, and H. U. Yee, Relativistic hydrodynamic fluctuations, *Phys. Rev. C* **100**, 024910 (2019).
 - [8] X. An, G. Basar, M. Stephanov, and H. U. Yee, Fluctuation dynamics in a relativistic fluid with a critical point, *Phys. Rev. C* **102**, 034901 (2020).
 - [9] P. C. Hohenberg and B. I. Halperin, Theory of dynamic critical phenomena, *Rev. Mod. Phys.* **49**, 435 (1977).
 - [10] D. T. Son and M. A. Stephanov, Dynamic universality class of the QCD critical point, *Phys. Rev. D* **70**, 056001 (2004).
 - [11] H. Fujii and M. Ohtani, Sigma and hydrodynamic modes along the critical line, *Phys. Rev. D* **70**, 014016 (2004).
 - [12] B. V. Jacak and B. Müller, The exploration of hot nuclear matter, *Science* **337**, 310 (2012).
 - [13] P. Braun-Munzinger, V. Koch, T. Schäfer, and J. Stachel, Properties of hot and dense matter from relativistic heavy ion collisions, *Phys. Rep.* **621**, 76 (2016).
 - [14] W. Busza, K. Rajagopal, and W. van der Schee, Heavy ion collisions: The big picture, and the big questions, *Annu. Rev. Nucl. Part. Sci.* **68**, 339 (2018).
 - [15] D. A. Teaney, Viscous hydrodynamics and the quark gluon plasma, in *Quark-Gluon Plasma* (World Scientific, Singapore, 2010), https://doi.org/10.1142/9789814293297_0004.
 - [16] B. Schenke, S. Jeon, and C. Gale, (3 + 1)D hydrodynamic simulation of relativistic heavy-ion collisions, *Phys. Rev. C* **82**, 014903 (2010).
 - [17] U. Heinz and R. Snellings, Collective flow and viscosity in relativistic heavy-ion collisions, *Annu. Rev. Nucl. Part. Sci.* **63**, 123 (2013).
 - [18] L. Del Zanna, V. Chandra, G. Inghirami, V. Rolando, A. Beraudo, A. De Pace, G. Pagliara, A. Drago, and F. Becattini, Relativistic viscous hydrodynamics for heavy-ion collisions with ECHO-QGP, *Eur. Phys. J. C* **73**, 2524 (2013).
 - [19] I. Karpenko, P. Huovinen, and M. Bleicher, A 3 + 1 dimensional viscous hydrodynamic code for relativistic heavy ion collisions, *Comput. Phys. Commun.* **185**, 3016 (2014).
 - [20] R. Derradi de Souza, T. Koide, and T. Kodama, Hydrodynamic approaches in relativistic heavy ion reactions, *Prog. Part. Nucl. Phys.* **86**, 35 (2016).
 - [21] P. Romatschke and U. Romatschke, *Relativistic fluid dynamics in and out of equilibrium* (Cambridge University Press, Cambridge, 2019), <https://doi.org/10.1017/9781108651998>.
 - [22] M. Connors, C. Nattrass, R. Reed, and S. Salur, Jet measurements in heavy ion physics, *Rev. Mod. Phys.* **90**, 025005 (2018).
 - [23] Y. Aoki, G. Endrodi, Z. Fodor, S. D. Katz, and K. K. Szabo, The order of the quantum chromodynamics transition

- predicted by the standard model of particle physics, *Nature (London)* **443**, 675 (2006).
- [24] M. M. Aggarwal *et al.* (STAR Collaboration), An experimental exploration of the QCD phase diagram: The search for the critical point and the onset of de-confinement, [arXiv:1007.2613](https://arxiv.org/abs/1007.2613).
- [25] B. Friman, C. Höhne, J. Knoll, S. Leupold, J. Randrup, R. Rapp, and P. Senger, The CBM physics book: Compressed baryonic matter in laboratory experiments, *Lect. Notes Phys.* **814**, 11 (2011).
- [26] X. Luo, Exploring the QCD phase structure with beam energy scan in heavy-ion collisions, *Nucl. Phys.* **A956**, 75 (2016).
- [27] A. Bzdak, S. Esumi, V. Koch, J. Liao, M. Stephanov, and N. Xu, Mapping the phases of quantum chromodynamics with beam energy scan, *Phys. Rep.* **853**, 1 (2020).
- [28] X. Luo, S. Shi, N. Xu, and Y. Zhang, A study of the properties of the QCD phase diagram in high-energy nuclear collisions, *Particles* **3**, 278 (2020).
- [29] K. Rajagopal and F. Wilczek, Static and dynamic critical phenomena at a second order QCD phase transition, *Nucl. Phys.* **B399**, 395 (1993).
- [30] J. Berges and K. Rajagopal, Color superconductivity and chiral symmetry restoration at nonzero baryon density and temperature, *Nucl. Phys.* **B538**, 215 (1999).
- [31] A. M. Halasz, A. D. Jackson, R. E. Shrock, M. A. Stephanov, and J. J. M. Verbaarschot, On the phase diagram of QCD, *Phys. Rev. D* **58**, 096007 (1998).
- [32] K. Fukushima and T. Hatsuda, The phase diagram of dense QCD, *Rep. Prog. Phys.* **74**, 014001 (2011).
- [33] K. Fukushima and C. Sasaki, The phase diagram of nuclear and quark matter at high baryon density, *Prog. Part. Nucl. Phys.* **72**, 99 (2013).
- [34] M. A. Stephanov, K. Rajagopal, and E. V. Shuryak, Signatures of the Tricritical Point in QCD, *Phys. Rev. Lett.* **81**, 4816 (1998).
- [35] M. A. Stephanov, K. Rajagopal, and E. V. Shuryak, Event-by-event fluctuations in heavy ion collisions and the QCD critical point, *Phys. Rev. D* **60**, 114028 (1999).
- [36] Y. Hatta and M. A. Stephanov, Proton Number Fluctuation as a Signal of the QCD Critical Endpoint, *Phys. Rev. Lett.* **91**, 102003 (2003).
- [37] M. Asakawa and M. Kitazawa, Fluctuations of conserved charges in relativistic heavy ion collisions: An introduction, *Prog. Part. Nucl. Phys.* **90**, 299 (2016).
- [38] X. Luo and N. Xu, Search for the QCD critical point with fluctuations of conserved quantities in relativistic heavy-ion collisions at RHIC: An overview, *Nucl. Sci. Tech.* **28**, 112 (2017).
- [39] L. Adamczyk *et al.* (STAR Collaboration), Energy Dependence of Moments of Net-Proton Multiplicity Distributions at RHIC, *Phys. Rev. Lett.* **112**, 032302 (2014).
- [40] J. Adam *et al.* (STAR Collaboration), Net-proton number fluctuations and the quantum chromodynamics critical point, [arXiv:2001.02852](https://arxiv.org/abs/2001.02852).
- [41] J. Adamczewski-Musch *et al.* (HADES Collaboration) Proton number fluctuations in $\sqrt{s_{NN}} = 2.4$ GeV Au + Au collisions studied with HADES, *Phys. Rev. C* **102**, 024914 (2020).
- [42] M. A. Stephanov, Non-Gaussian Fluctuations Near the QCD Critical Point, *Phys. Rev. Lett.* **102**, 032301 (2009).
- [43] M. Asakawa, S. Ejiri, and M. Kitazawa, Third Moments of Conserved Charges as Probes of QCD Phase Structure, *Phys. Rev. Lett.* **103**, 262301 (2009).
- [44] M. A. Stephanov, On the Sign of Kurtosis Near the QCD Critical Point, *Phys. Rev. Lett.* **107**, 052301 (2011).
- [45] B. Berdnikov and K. Rajagopal, Slowing out-of-equilibrium near the QCD critical point, *Phys. Rev. D* **61**, 105017 (2000).
- [46] M. Nahrgang, S. Leupold, C. Herold, and M. Bleicher, Nonequilibrium chiral fluid dynamics including dissipation and noise, *Phys. Rev. C* **84**, 024912 (2011).
- [47] M. Nahrgang, S. Leupold, and M. Bleicher, Equilibration and relaxation times at the chiral phase transition including reheating, *Phys. Lett. B* **711**, 109 (2012).
- [48] M. Nahrgang, C. Herold, S. Leupold, I. Mishustin, and M. Bleicher, The impact of dissipation and noise on fluctuations in chiral fluid dynamics, *J. Phys. G* **40**, 055108 (2013).
- [49] C. Herold, M. Nahrgang, I. Mishustin, and M. Bleicher, Chiral fluid dynamics with explicit propagation of the Polyakov loop, *Phys. Rev. C* **87**, 014907 (2013).
- [50] M. Nahrgang, C. Herold, and M. Bleicher, Influence of an inhomogeneous and expanding medium on signals of the QCD phase transition, *Nucl. Phys.* **A904-905**, 899c (2013).
- [51] C. Herold, M. Nahrgang, Y. Yan, and C. Kobdaj, Net-baryon number variance and kurtosis within nonequilibrium chiral fluid dynamics, *J. Phys. G* **41**, 115106 (2014).
- [52] S. Mukherjee, R. Venugopalan, and Y. Yin, Real time evolution of non-Gaussian cumulants in the QCD critical regime, *Phys. Rev. C* **92**, 034912 (2015).
- [53] C. Herold, M. Nahrgang, Y. Yan, and C. Kobdaj, Dynamical net-proton fluctuations near a QCD critical point, *Phys. Rev. C* **93**, 021902 (2016).
- [54] M. Nahrgang and C. Herold, Phenomena at the QCD phase transition in nonequilibrium chiral fluid dynamics (N_{χ} FD), *Eur. Phys. J. A* **52**, 240 (2016).
- [55] S. Mukherjee, R. Venugopalan, and Y. Yin, Universal Off-Equilibrium Scaling of Critical Cumulants in the QCD Phase Diagram, *Phys. Rev. Lett.* **117**, 222301 (2016).
- [56] C. Herold, M. Bleicher, M. Nahrgang, J. Steinheimer, A. Limphirat, C. Kobdaj, and Y. Yan, Broadening of the chiral critical region in a hydrodynamically expanding medium, *Eur. Phys. J. A* **54**, 19 (2018).
- [57] M. Stephanov and Y. Yin, Hydrodynamics with parametric slowing down and fluctuations near the critical point, *Phys. Rev. D* **98**, 036006 (2018).
- [58] C. Herold, A. Kittiratpattana, C. Kobdaj, A. Limphirat, Y. Yan, M. Nahrgang, J. Steinheimer, and M. Bleicher, Entropy production and reheating at the chiral phase transition, *Phys. Lett. B* **790**, 557 (2019).
- [59] K. Rajagopal, G. Ridgway, R. Weller, and Y. Yin, Hydro+ in action: Understanding the out-of-equilibrium dynamics near a critical point in the QCD phase diagram, [arXiv:1908.08539](https://arxiv.org/abs/1908.08539) [Phys. Rev. D (to be published)].
- [60] L. Du, U. Heinz, K. Rajagopal, and Y. Yin, Fluctuation dynamics near the QCD critical point, [arXiv:2004.02719](https://arxiv.org/abs/2004.02719).
- [61] M. Kitazawa, M. Asakawa, and H. Ono, Non-equilibrium time evolution of higher order cumulants of conserved

- charges and event-by-event analysis, *Phys. Lett. B* **728**, 386 (2014).
- [62] M. Sakaida, M. Asakawa, and M. Kitazawa, Effects of global charge conservation on time evolution of cumulants of conserved charges in relativistic heavy ion collisions, *Phys. Rev. C* **90**, 064911 (2014).
- [63] M. Sakaida, M. Asakawa, H. Fujii, and M. Kitazawa, Dynamical evolution of critical fluctuations and its observation in heavy ion collisions, *Phys. Rev. C* **95**, 064905 (2017).
- [64] M. Nahrgang, M. Bluhm, T. Schäfer, and S. A. Bass, Baryon number diffusion with critical fluctuations, *Nucl. Phys. A* **967**, 824 (2017).
- [65] M. Nahrgang, M. Bluhm, T. Schäfer, and S. A. Bass, Diffusive dynamics of critical fluctuations near the QCD critical point, *Phys. Rev. D* **99**, 116015 (2019).
- [66] M. Bluhm, Y. Jiang, M. Nahrgang, J. Pawłowski, F. Rennecke, and N. Wink, Time-evolution of fluctuations as signal of the phase transition dynamics in a QCD-assisted transport approach, *Nucl. Phys. A* **982**, 871 (2019).
- [67] Y. Akamatsu, D. Teaney, F. Yan, and Y. Yin, Transits of the QCD critical point, *Phys. Rev. C* **100**, 044901 (2019).
- [68] M. Bluhm and M. Nahrgang, Time-evolution of net-baryon density fluctuations across the QCD critical region, [arXiv:1911.08911](https://arxiv.org/abs/1911.08911).
- [69] M. Bluhm *et al.*, Dynamics of critical fluctuations: Theory phenomenology heavy-ion collisions, *Nucl. Phys. A* **1003**, 122016 (2020).
- [70] C. Nonaka and M. Asakawa, Hydrodynamical evolution near the QCD critical end point, *Phys. Rev. C* **71**, 044904 (2005).
- [71] M. Bluhm and B. Kämpfer, Quasi-particle perspective on critical end-point, *Proc. Sci., CPOD2006* (2006) 004.
- [72] P. Parotto, M. Bluhm, D. Mroczek, M. Nahrgang, J. Noronha-Hostler, K. Rajagopal, C. Ratti, T. Schäfer, and M. Stephanov, QCD equation of state matched to lattice data and exhibiting a critical point singularity, *Phys. Rev. C* **101**, 034901 (2020).
- [73] C. Young, Numerical integration of thermal noise in relativistic hydrodynamics, *Phys. Rev. C* **89**, 024913 (2014).
- [74] K. Murase and T. Hirano, Hydrodynamic fluctuations and dissipation in an integrated dynamical model, *Nucl. Phys. A* **956**, 276 (2016).
- [75] M. Nahrgang, M. Bluhm, T. Schäfer, and S. Bass, Toward the description of fluid dynamical fluctuations in heavy-ion collisions, *Acta Phys. Pol. B Proc. Suppl.* **10**, 687 (2017).
- [76] M. Bluhm, M. Nahrgang, T. Schäfer, and S. A. Bass, Fluctuating fluid dynamics for the QGP in the LHC and BES era, *EPJ Web Conf.* **171**, 16004 (2018).
- [77] M. Singh, C. Shen, S. McDonald, S. Jeon, and C. Gale, Hydrodynamic fluctuations in relativistic heavy-ion collisions, *Nucl. Phys. A* **982**, 319 (2019).
- [78] T. Hirano, R. Kurita, and K. Murase, Hydrodynamic fluctuations of entropy in one-dimensionally expanding system, *Nucl. Phys. A* **984**, 44 (2019).
- [79] A. Sakai, K. Murase, and T. Hirano, Rapidity decorrelation of anisotropic flow caused by hydrodynamic fluctuations, [arXiv:2003.13496](https://arxiv.org/abs/2003.13496).
- [80] J. B. Bell, A. L. Garcia, and S. A. Williams, Numerical methods for the stochastic Landau-Lifshitz Navier-Stokes equations, *Phys. Rev. E* **76**, 016708 (2007).
- [81] A. Donev, E. Vanden-Eijnden, A. L. Garcia, and J. B. Bell, On the accuracy of finite-volume schemes for fluctuating hydrodynamics, [arXiv:0906.2425](https://arxiv.org/abs/0906.2425).
- [82] J. A. de la Torre, P. Español, and A. Donev, Finite element discretization of non-linear diffusion equations with thermal fluctuations, *J. Chem. Phys.* **142**, 094115 (2015).
- [83] M. M. Tsypin, Universal Effective Potential for Scalar Field Theory in Three-Dimensions by Monte Carlo Computation, *Phys. Rev. Lett.* **73**, 2015 (1994).
- [84] M. M. Tsypin, Effective potential for a scalar field in three dimensions: Ising model in the ferromagnetic phase, *Phys. Rev. B* **55**, 8911 (1997).
- [85] R. Guida and J. Zinn-Justin, 3-D Ising model: The scaling equation of state, *Nucl. Phys. B* **489**, 626 (1997).
- [86] M. Agah Nohou, M. Bluhm, A. Borer, M. Nahrgang, T. Sami, and N. Touroux, Finite size effects on cumulants of the critical mode, *Proc. Sci., CORFU2018* (2019) 179.
- [87] J. Randrup and J. Cleymans, Exploring high-density baryonic matter: Maximum freeze-out density, *Eur. Phys. J. C* **52**, 218 (2016).
- [88] L. V. Bravina, I. Arsene, M. S. Nilsson, K. Tywoniuk, E. E. Zabrodin, J. Bleibel, A. Faessler, C. Fuchs, M. Bleicher, G. Baur, and H. Stöcker, Microscopic models and effective equation of state in nuclear collisions at FAIR energies, *Phys. Rev. C* **78**, 014907 (2008).
- [89] M. Bluhm, M. Nahrgang, S. A. Bass, and T. Schäfer, Impact of resonance decays on critical point signals in net-proton fluctuations, *Eur. Phys. J. C* **77**, 210 (2017).
- [90] M. Bluhm, M. Nahrgang, S. A. Bass, and T. Schäfer, Behavior of universal critical parameters in the QCD phase diagram, *J. Phys. Conf. Ser.* **779**, 012074 (2017).
- [91] M. Kitazawa, G. Pihan, N. Touroux, M. Bluhm, and M. Nahrgang, Critical fluctuations in a dynamically expanding heavy-ion collision, [arXiv:2002.07322](https://arxiv.org/abs/2002.07322).